Progenitors of Type Ia Supernovae

by

Cody Raskin

A Dissertation Presented in Partial Fulfillment
of the Requirements for the Degree
Doctor of Philosophy

Approved April 2011 by the
Graduate Supervisory Committee:

Evan Scannapieco, Chair
James Rhoads
Patrick Young
Allen McNamara
Francis Timmes

ARIZONA STATE UNIVERSITY

May 2011

ABSTRACT

Type Ia supernovae are important, but mysterious cosmological tools. Their standard brightnesses have enabled cosmologists to measure extreme distances and to discover dark energy. However, the nature of their progenitor mechanisms remains elusive, with many competing models offering only partial clues to their origins. Here, type Ia supernova delay times are explored using analytical models. Combined with a new observation technique, this model places new constraints on the characteristic time delay between the formation of stars and the first type Ia supernovae. This derived delay time (500 million years) implies low-mass companions for single degenerate progenitor scenarios.

In the latter portions of this dissertation, two progenitor mechanisms are simulated in detail; white dwarf collisions and mergers. From the first of these simulations, it is evident that white dwarf collisions offer a viable and unique pathway to producing type Ia supernovae. Many of the combinations of masses simulated produce sufficient quantities of ^{56}Ni (up to 0.51 solar masses) to masquerade as normal type Ia supernovae. Other combinations of masses produce ^{56}Ni yields that span the entire range of supernova brightnesses, from the very dim and underluminous, with 0.14 solar masses, to the over-bright and superluminous, with up to 1.71 solar masses. The ^{56}Ni yield in the collision simulations depends non-linearly on total system mass, mass ratio, and impact parameter.

Using the same numerical tools as in the collisions examination, white dwarf mergers are studied in detail. Nearly all of the simulations produce merger remnants consisting of a cold, degenerate core surrounded by a hot accretion disk. The properties of these disks have strong implications for various viscosity treatments that have attempted to pin down the accretion times. Some mass combinations produce super-Chandrasekhar cores on shorter time scales than viscosity driven accretion. A handful of simulations also exhibit helium detonations on the surface of the primary that bear a resemblance to helium novae.

Finally, some of the preliminary groundwork that has been laid for constructing a new numerical tool is discussed. This new tool advances the merger simulations further than any research group has done before, and has the potential to answer some of the lingering questions that the merger study has uncovered. The results of thermal diffusion tests using this tool have a remarkable correspondence to analytical predictions.

i

Most importantly, however, I'd like to thank my wife, Elizabeth, for her support throughout my graduate career. There was a time that I considered a PhD as too lofty a goal to attain, and too impractical to pursue while starting a family. She convinced me that I could not truly be happy unless I gave every effort to fulfill my dreams of eventually becoming a professor. And in my daughter, Madeline, I have someone to make proud to call me "dad".

TABLE OF CONTENTS

LIST OF TABLES

LIST OF FIGURES

x

Chapter 1

INTRODUCTION

Late one night in 1572, a young Tycho Brahe walked out of Herrevad Abbey in Denmark to gaze at the night sky, as he often did, and remarked upon a bright new star in the constellation Cassiopeia. Since the universal assumption from the time of Aristotle was that the celestial sphere beyond the Moon and planets was immutable, surely this new star did not belong to the population of ordinary stars that resided far beyond them. The planets, as was known since antiquity, exhibited a parallax, or a relative motion with respect to the background stars over periods of days to months, and this new star was certainly bright enough to be a planet, appearing brighter even than Venus. Tycho Brahe, perhaps surmising that this new star might not be a planet, was so intrigued by this peculiar object that he built his own sextant in the hopes to observe its parallax and carefully measured its position nearly every night for the next year. And while the star had dimmed slightly over this time, much to his delight, it appeared not to move relative to the background stars. This placed it firmly among the stars, and he dubbed it a "stella nova" - the latin phrase for "new star."

Tycho's observations of this object made him world-famous and heralded the beginning of a new era of precision astronomy that has persisted to this day. We now know that Tycho's new star was actually a supernova (SN1572), and in particular, a unique class of supernovae called a type Ia supernova. The light from that cataclysm, observed so many centuries ago, has been echoing across the galaxy and back to us ever since (Krause et al. 2008), and the remnant is still visible today with powerful telescopes (see Figure 1.1).

1.1   Type Ia Supernovae as Cosmological Tools

Type Ia supernovae (SNeIa) are thought to be responsible for the largest contribution of iron-group elements to the early universe (Wheeler et al.1989; Timmes et al. 1995; Feltzing et al. 2001; Strigari 2006), and they serve as direct probes of low-mass star formation rates at high red-shift (Scannapieco & Bildsten 2005; Mannucci et al. 2006; Maoz 2008). In addition, they have the remarkable property of being (nearly) standard candles. That is, their intrinsic brightnesses can be inferred from other properties of their lightcurves (Phillips 1993). When the intrinsic brightness of an object is known, its apparent brightness is then only a function of its distance, and so SNeIa are routinely used to calculate extreme distances for cosmological measurements
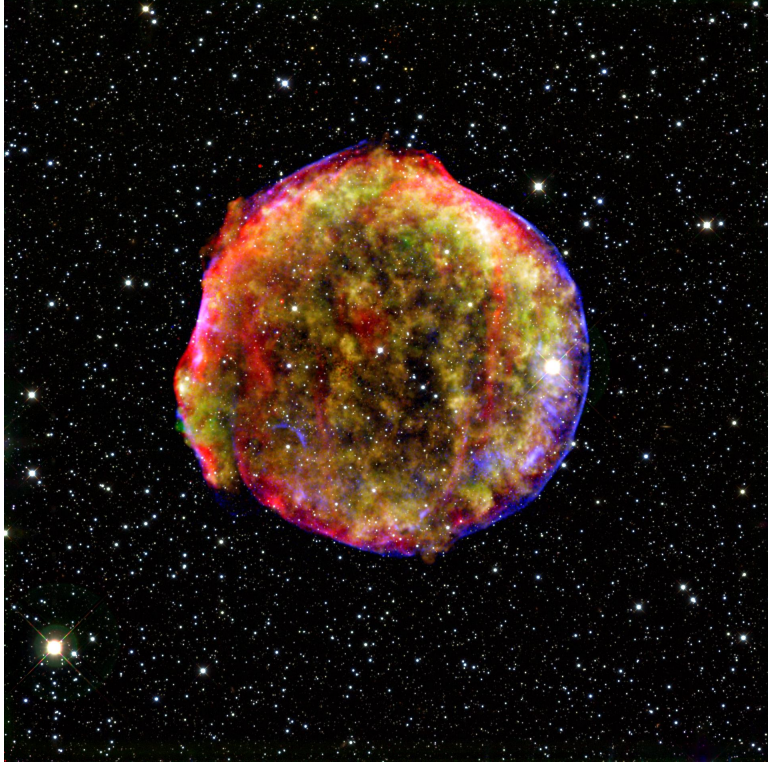
Figure 1.1: Composite image of the remnant of SN 1572 as seen by Chandra X-Ray Observatory, Spitzer Space Telescope, and Calar Alto Observatory.

(Branch & Tammann 1992). Measurements made from SNeIa distance calculations led to the discovery of the acceleration of the universe's expansion, revitalizing the concept of a cosmological constant or dark energy. However, the nature and history of the dark energy remains elusive.

A significant complication for performing cosmology with SNeIa is the uncertainty in the brightness measurements, especially at high redshift. Though the Phillips relation provides a guide to deriving their brightnesses, there are a number of systematic errors that creep into the observations and not all SNeIa fit the standardizing templates. The result is that SNeIa measurements lack the precision necessary to shed light on any of the major mysteries that the existence of dark energy has uncovered (see Figure 1.2 showing distance vs. Hubble residuals).

We might achieve this precision were it not for the fact that as of yet, the astrophysical community lacks a clear understanding of the exact mechanism responsible for producing SNeIa. While the basic constituents are known, there are many competing theories of the dynamics that lead to the supernova, of the nature of the detonation, of the interaction of the supernova ejecta
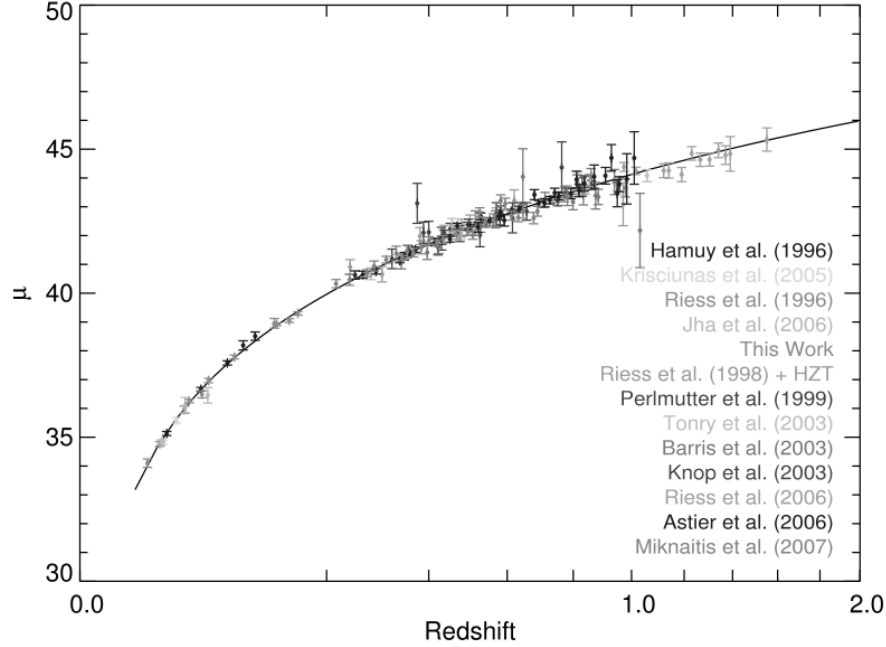
Figure 1.2: A hubble diagram drawing from several SNeIa observations. The errors in the Hubble residuals become quite large at high redshift. Reproduced from Kowalski et al. (2008).

with circumstellar gas, and of the physics responsible for making SNeIa standardizable at all. If SNeIa are to remain useful for cosmology, all of these variables will need to be understood in the context of a progenitor mechanism with high predictive value.

1.2 White Dwarf Stars & Progenitor Mechanisms

When a typical star nears the end of its life, it will have burned much of its hydrogen into helium, and for a star larger than roughly 1.5 solar masses ($1.5\,M_{\odot}$), much of that helium into carbon and oxygen. These burning products settle by gravity into the core of the star where no further burning occurs if the star is less than $8\,M_{\odot}$. Without nuclear energy generation to halt the contraction due to gravity, the core material collapses into an ever smaller volume until Pauli's exclusion principle, which holds that no two electrons may occupy the same quantum state, prevents any further collapse. The absence of free quantum states (or in other words, the filling of all quantum states) in any system is called degeneracy. The material that comprises the core of a star at this stage is said to be in a degenerate state, as it is the electron degeneracy pressure that is supporting it against further collapse from gravity. As the star sheds its outer layers, this degenerate core remains as a white dwarf star and shines with residual thermal

energy for billions of years, but is otherwise an inert object.

White dwarf stars have a number of peculiar features. Foremost among them is their unintuitive mass-radius relation. We may derive an approximation of this relation by requiring that the star is in pressure equilibrium. This implies that the gravitational potential energy per unit mass,

$$E_g \approx \frac{-GM}{R}, \tag{1.1}$$

where M is the total mass of the star and R is the radius, is equal in magnitude to the total kinetic energy per unit mass. The kinetic energy of a unit mass of degenerate gas in a white dwarf derives from the motions of each of its electrons ($E_e = p^2/2m_e$). Since the electrons are finely constrained in degenerate gas, we may approximate their momentum to be of order the uncertainty in their momentum (i.e. $p \sim \Delta p = \hbar^2 \Delta x^{-1}$). With not much room for these electrons to move, Δx will be of order the average inter-electron spacing, or $n^{-1/3}$, where n is the number density of electrons. This total kinetic energy per unit mass is then

$$E_k \approx N \frac{\Delta p^2}{2m_e} \approx N \frac{\hbar^2 n^{2/3}}{2m_e} \approx N^{5/3} \frac{M^{2/3} \hbar^2}{2m_e R^2}, \tag{1.2}$$

where N is the total number of electrons per unit mass and m_e is the mass of an electron. Setting these energies equal to each other ($|E_g| = E_k$) yields

$$\begin{aligned} \frac{GM}{R} &= N^{5/3} \frac{M^{2/3} \hbar^2}{2m_e R^2}, \\ R &= \frac{N^{5/3} \hbar^2}{2m_e G M^{1/3}}. \end{aligned} \tag{1.3}$$

Since N depends only on the isotopic composition of the white dwarf, this implies an approximate scaling relationship between radius and mass of $R \propto M^{-1/3}$.

This remarkable conclusion implies that when a white dwarf grows more massive, it actually becomes physically smaller. Indeed, while the most common white dwarfs with a mass of $0.6\,M_\odot$ have a radius about the same as the Earth, $R \approx 0.01 R_\odot$, the most massive white dwarfs, nearing $1.4\,M_\odot$ are only 3/4 as large. This mass-radius scaling relation will become important in subsequent chapters as it governs much of the dynamics of how white dwarfs interact.

A second peculiarity of white dwarf stars is that in being composed of degenerate gas, they do not respond to thermodynamic changes like an ideal gas. With their pressure support deriving entirely from electron degeneracy, changes in temperature are not reflected in changes

in pressure. In fact, the equation of state for a white dwarf can be more aptly approximated as $P \propto \rho^\gamma$, where γ is a parameter that relates to the degree of degeneracy. In practice, with pressure scaling only with density, this means that strong temperature fluctuations that incite nuclear burning of degenerate gas will quickly run away, as the thermal energy produced by the burning raises the temperature of the gas, but the gas does not respond by expanding, cooling and quenching the burn. As the temperature rises, the nuclear burning rates increase, and what was a slight increase in temperature rapidly evolves into a catastrophic detonation.

A type Ia supernova is the observed transient after the thermonuclear detonation of one (or more) of these white dwarf stars. The light it produces is powered by the radioactive decay of ^{56}Ni (a product of intense carbon-burning) to ^{56}Co, and subsequently to ^{56}Fe. Its spectra is characterized by a lack of hydrogen and helium lines, distinguishing it from type II and type Ib supernovae, respectively, and by a singly-ionized silicon line at 6150Å, distinguishing it from a type Ic supernova. These features together strongly support the idea that the progenitor star is a carbon-oxygen white dwarf, devoid of any hydrogen or helium. Several features of SNeIa spectra also suggest that there is a protracted deflagration phase before the detonation, where carbon and oxygen are burned more slowly than in an outright detonation. How an otherwise inert white dwarf star, that is typically not subject to any temperature fluctuations, detonates in this fashion is hotly debated and several competing models exist.

The most commonly accepted progenitor model consists of a single white dwarf star accreting helium gas from an evolved, late-stage companion star like a red giant or asymptotic giant branch star (Whelan & Iben 1973; Nomoto 1982; Hillebrandt & Niemeyer 2000), as is depicted in Figure 1.3. In this accretion model, the white dwarf will grow in mass until it reaches what is called the Chandrasekhar limit, the maximum allowable mass for a white dwarf star ($\approx 1.4\,M_\odot$; Chandrasekhar 1931). This would seem to be a natural explanation for the Phillips relation, since a progenitor mechanism that requires the same white dwarf mass every time removes one of the most confounding free parameters. However, there are a number of theoretical hurdles for this model.

First, it is not clear that pushing a white dwarf up to the Chandrasekhar limit can always produce a type Ia supernova. In fact, it may be much more likely that a white dwarf at this limit, where electron degeneracy pressure can no longer support gravity, will simply collapse to form a neutron star. The likelihood for so-called "accretion induced collapse" was explored
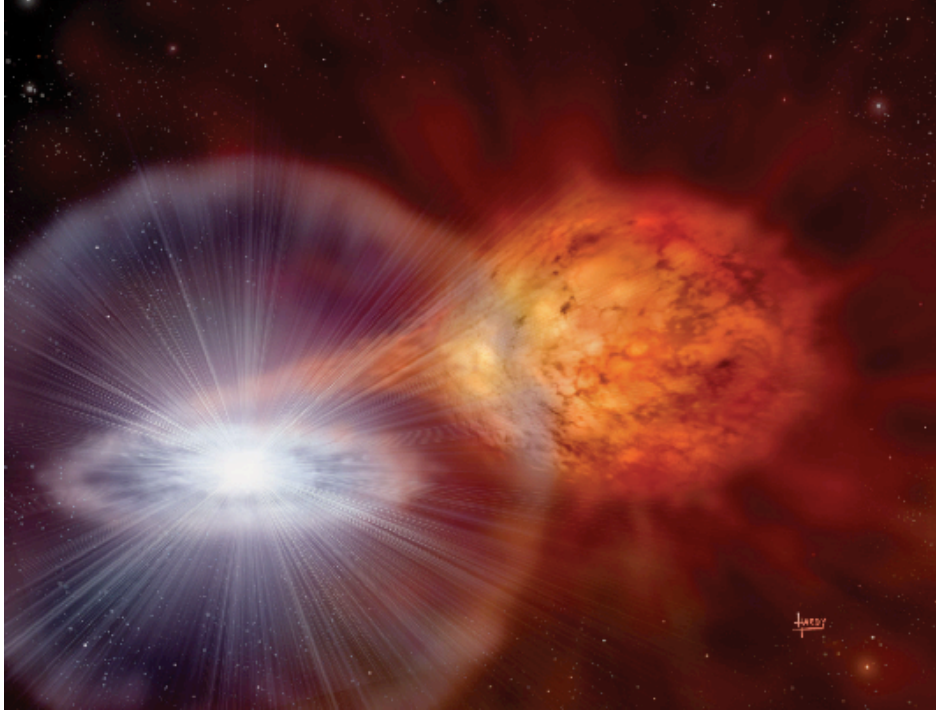
Figure 1.3: An artist's depiction of a white dwarf star (left) accreting gas from an evolved companion (right). ©David A. Hardy.

in detail by Nomoto & Kondo (1991). Second, there are several observations that suggest this mechanism cannot be responsible for every type Ia supernova. Observations of SN2007if by Scalzo et al. (2010) and of SN2009dc by Tanaka et al. (2010), suggest $1.6 \pm 0.1\,M_\odot$ and $1.2\,M_\odot$ of ^{56}Ni, respectively. Observations of SN2003fg by Howell et al. (2006) and of SN2006gz by Hicken et al. (2007) both suggest ^{56}Ni yields of $\approx 1.3\,M_\odot$. All of these yields are far too great to have been generated by the detonation of a single, Chandrasekhar-mass white dwarf. Instead, it is suggested that these SNeIa arose out of double-degenerate scenarios; progenitor mechanisms involving two white dwarf stars.

By contrast, in double-degenerate models, two white dwarfs merge or collide, triggering a detonation and subsequent supernova. These models have the benefit of having much more relaxed mass constraints. In fact, the Chandrasekhar mass isn't a factor in as much as these models are able to replicate supernovae with a range of progenitor masses extending from as little as $0.5\,M_\odot$ up to $1.4\,M_\odot$ for one of a pair of white dwarfs. The bulk of this thesis focuses on exploring two double-degenerate models - collisions and mergers - as possible progenitors for SNeIa. While it is not clear how common double-degenerate SNeIa progenitors are as compared

to single-degenerate progenitors, double-degenerate models have the potential to answer many of the outstanding questions about peculiar SNeIa, as the supernovae they produce span the brightness range from very dim "point-Ia"-like SNe, to the overluminous SNeIa with super-Chandrasekhar masses of ^{56}Ni.

What is clear from the observed supernova rates is that whatever the mechanisms that are ultimately responsible for producing SNeIa, nearly 1% of all white dwarf stars ever formed must be converted to SNeIa. This is a staggeringly high conversion rate and suggests the culprit mechanisms are robust. That is, a wide range of parameters must lead to the same basic result.

In this thesis, I intend to describe the work I have done to illuminate some of the properties of SNeIa progenitors in the hopes of providing clues that explain some of the peculiarities of SNeIa and allow for better distance measurements that employ them. Starting with chapter 2, I describe an observational project that measured the characteristic time delay between the formation of stars and the onset of SNeIa. This time delay reveals important details about the age and possible progenitor masses of the white dwarfs that eventually lead to SNeIa and has significant implications for the competing progenitor scenarios. In chapters 3 and 4, I describe two ground-breaking simulation studies modeling double-degenerate collisions and mergers. Many of these simulations are the first of their kind and have opened the door onto a new avenue for SNeIa research. In chapter 5, I discuss what lies ahead for future SNeIa progenitor studies and which mysteries might be solved sooner than others.

Chapter 2

PROMPT IA SUPERNOVAE ARE SIGNIFICANTLY DELAYED

The time delay between the formation of a population of stars and the onset of type Ia super-novae sets important limits on the masses and nature of SNeIa progenitors. Before investigated the plausibility of particular progenitor mechanisms, we first examine this delay time in detail. Since SNeIa may have a range of time delays, much work has been dedicated to mapping out their delay-time distribution (DTD). However, the characteristic delay time is often simpler to measure and can provide a more general framework for developing progenitor mechanism theories. In this chapter, we describe a new observational technique to measure the characteristic time delay of the DTD by comparing the spatial distributions of SNeIa to their local environments. Previous work attempted such analyses encompassing the entire host of each SNIa, yeilding inconclusive results. Our approach confines the analysis only to the relevant portions of the hosts, allowing us to show that even so-called "prompt" SNeIa that trace star-formation on cosmic timescales exhibit a significant delay time of 200-500 million years. This implies that either the majority of SNeIa companion stars have main-sequence masses less than $3\,M_\odot$, or that most SNeIa arise from double-white dwarf binaries. This conclusion has important implications for the work that will be discussed in later chapters. The results here are also consistent with a SNeIa rate that traces the white dwarf formation rate, scaled by a fixed efficiency factor.

2.1 Introduction

Type Ia supernovae serve as the primary cosmological standard candles (Colgate 1979; Branch & Tammann 1992; Phillips 1993), due to their extremely regular light curves (Pskovskii 1977; Phillips 1993). However, this regularity need not imply that they share a common progenitor. Indeed, one striking bimodality is that the brightest SNeIa occur in star-forming galaxies, and the dimmest SNeIa occur in galaxies with little star-formation (Hamuy et al. 1996; Howell 2001; van den Bergh & Filippenko 2005). This points to an evolution of SNeIa progenitors, and in fact, while several parameterizations of the SNeIa rate exist (Greggio & Renzini 1983; Kobayashi et al. 2000; Greggio 2005), current data is well fit by a two-component parameterization (Mannucci et al. 2005; Scannapieco & Bildsten 2005), which takes the form

$$SNR_{\mathrm{Ia}}(t) = AM_*(t) + B\dot{M}_*(t). \tag{2.1}$$

Here, we refer to the A-component, which is proportional to the total stellar mass of the host, as delayed, and to the B-component, which is is proportional to the instantaneous star-formation rate, as prompt. Note that these words have been occasionally used slightly differently in the literature (Greggio & Renzini 1983; Mannucci et al. 2006), assigning SNeIa as prompt or delayed/tardy based on timescales, rather than the parameterization in eq. (1).

Despite the usefulness of eq. (1) on long time scales, there are several reasons to believe that the prompt component should not be pinned to the instantaneous star-fomation rate. If core-collapse supernovae (SNcc) and prompt SNeIa occured simultaneously, the oldest stars in the Milky Way would be much more strongly enriched with iron group elements than observed (McWilliams 1992; Scannapieco & Bildsten 2005). Furthermore, unlike SNcc, SNeIa can not arise before stars evolve to form white-dwarfs, which takes at least 40 Myrs. Thus, it is likely that the prompt component exhibits its own delay time, τ, such that $SNR_{\mathrm{Ia}}(t) = AM_*(t) + B\dot{M}_*(t - \tau)$, where current constraints, which use the global properties of host galaxies, place an indirect upper limit of $\tau \leq 500$ Myr on this timescale (Dahlen et al. 2004; Gal-Yam & Maoz 2004; Mannucci et al. 2005; Scannapieco & Bildsten 2005; Sullivan et al. 2006; Dilday et al. 2008). Galaxies older than this age have fewer SNeIa, suggesting the characteristic delay time of the prompt component cannot be longer than 500 Myr. An alternative model is that SNeIa occur at a rate that is directly proportional to the white dwarf formation rate (WDFR). In particular, Pritchet et al. (2008) argue for a uniform conversion of newly formed white dwarfs into type SNeIa at an efficiency of $\approx 1\%$, matching the observed rates of SNeIa. This would fix the Ia rate as being proportional to the stellar death rate of stars less than $8\,M_\odot$.

In this chapter, we employ a new observational technique measuring the spatial distributions of SNeIa and compare the results to analytical models with the goal of constraining the delay time, τ, for the B-component in the A+B formalism, and the feasability of the white dwarf formation rate (WDFR) model. The structure of this chapter is as follows. In §2, we review previous work constraining the progenitors of other classes of transients, and build on these techniques to develop a new analysis applicable to type Ia SNe. In §3, we review the construction of the analytical host model for comparison from Raskin et al. (2008), including modifications necessary to make accurate comparisons to the results of our new observational technique. We present our results of the analysis and comparisons in §4, and conclusions are given in §5.

2.2 Data and Analysis
Previous work

Fruchter et al. (2006) developed an observational approach in which, for each host galaxy, they computed the fraction of the total light (or photon counts) in all pixels fainter than the pixel containing a transient. By compiling a sample of such measurements into a cumulative histogram, they demonstrated that long-duration gamma-ray bursts are more likely than SNcc to cluster in the brighter regions of a galaxy. Kelly et al. (2008) expanded upon this analysis to distinguish between SNcc subtypes Ic, Ib, and type II (see also Anderson & James 2008).

However, this study showed no difference between SNcc and SNeIa, even though SNcc arise from massive, short-lived stars rather than from white dwarfs that form from longer-lived stars. In fact, both populations followed the same distribution as that of the g-band light. In the core-collapse case, this is because young stars lead both to supernovae and the brightest regions. On the other hand, SNeIa are not likely to arise from ongoing star formation, but they nevertheless share the same radial exponential profile as the g-band light, which is caused by a radially-decreasing density of stars. This radial gradient is large enough to obscure any signal caused by a delay in the prompt component (Raskin et al. 2008).

Doughnut Method

What is needed is a procedure that correlates SNeIa with the properties of nearby regions, rather than with the host as a whole. In a spiral host, the ideal method for constraining SNIa progenitors would be to measure the relative brightness of pixels within annuli. In this case, as the density wave of star-formation moves around each annulus, SNeIa would appear behind it at a characteristic surface brightness determined by the level to which a stellar population fades away in the g-band before SNeIa appear. The g-band is ideal for this analysis as it fades away on the order of 100 Myrs, a similar time as that of white dwarf formation. However, observations are never perfect, and observing a single annulus of a spiral host is subject to complications such as spurs, knots, and gaps, as well as the fact that stars rarely follow circular orbits.

We call our solution to this problem the doughnut method, and it builds directly on the method described in Fruchter et al. (2006). The idea is to expand an annulus radially by some small but appreciable radius, so as to encompass enough of the host's morphological peculiarities

Figure 2.1: A sample image showing a spiral host, NGC 3892, with a doughnut constraint, having a width of one-half the scale radius of the galaxy. The highlighted region has a small radial gradient, but still samples an area in which stars have an appreciable spread in ages reflected in their g-band surface brightnesses. The cross marks the location of type Ia supernova 1963J.

to have a good representative sample, yet narrow enough to represent local variations in the host light. Figure 1 illustrates this concept.

Sample Selection

Our sample was drawn from the the Padova-Asiago Supernova Catalogue (Barbon et al. 1999), by selecting those events occurring within $z < 0.07$ spiral hosts with Sloan Digital Sky Survey (SDSS) g-band images. While this yielded 98 SNeIa, we also removed those that occurred within $2''$ of a foreground star or within a galaxy inclined more than $60°$ or involved in a merger. This resulted in 50 usable images, and as a control sample, we also selected all SNcc meeting these criteria, which resulted in 74 usable images.

Note that before the advent of CCD astronomy, it was difficult to spot a supernova against the background light when it occurred near the bright center of its host galaxy (see Shaw 1979). This induces a bias in most SN catalogs, the effect of which is to count fewer supernovae at small radii than would be expected from the stellar distribution in the hosts (e.g. Howell et al. 2000). Figure 2.2 shows the radial distribution of SNeIa in our sample, which indicates a minor deficiency at small radii when our sample is compared to an exponential density distribution. Thankfully, our doughnut method overcomes this bias since it relies only

11
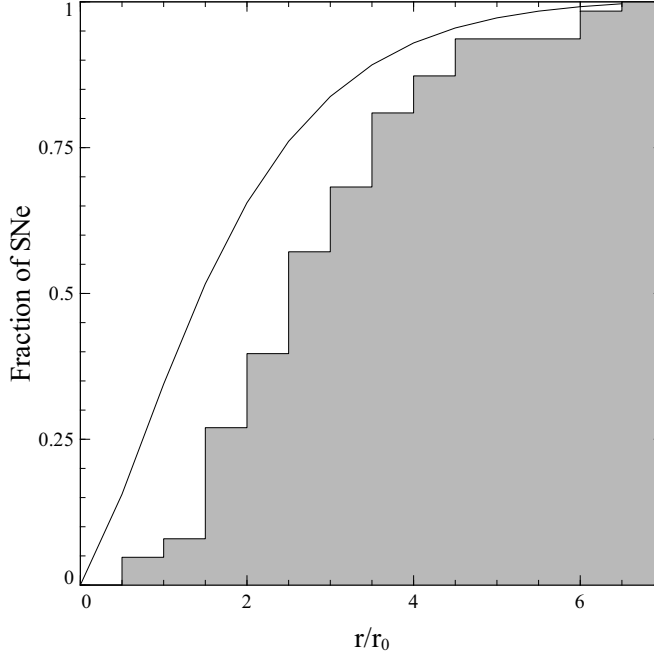
Figure 2.2: A cumulative histogram of the number of SNeIa vs. radial coordinate showing a deficit at small radii when compared to an exponential density distribution. Note that while the density of stars in a spiral host follows an exponential radial profile, the projected area scales as the square of the radius, resulting in 0 SN counts at the very center.

on the local environment of the transient. Constraining our sample, then, to only recently discovered SNe has little to no effect on our results. On the other hand, when global properties are considered, as in a traditional Fruchter et al. (2006) analysis, this bias can have drastic effects on the conclusions about SNeIa progenitors.

Given the typical resolution of SDSS images and the distances to these hosts, we settled on a doughnut width of $0.5r_0$, or $0.25r_0$ on either side of the transient, where r_0 is the scale radius. Host deprojection was carried out using the 25th mag B-band isophote as measured by the Padova-Asiago group, and to obtain the weighted average brightness within the uncertainties in the supernova location, we applied a gaussian convolution with $\sigma = 1.2''$. Figure 2.3 shows the cumulative supernova distribution vs. the cumulative light distribution. Unlike analyses that use the full galaxy light, our approach is able to distinguish between the SNcc and SNeIa distributions with 99.6% confidence, as quantified by a Kolmogorov-Smirnov (KS) test. SNeIa are clearly biased to fainter pixels, while the SNcc distribution closely follows the g-band light distribution.

In order to interpret this separation of the SNeIa from the SNcc data, we construct

12

an analytical model of a spiral galaxy following that of Raskin et al. (2008) with the necessary modifications to account for the doughnut method. Such a model allows us to age date the SNeIa by reproducing spatial distributions for a range of SNeIa delay times.
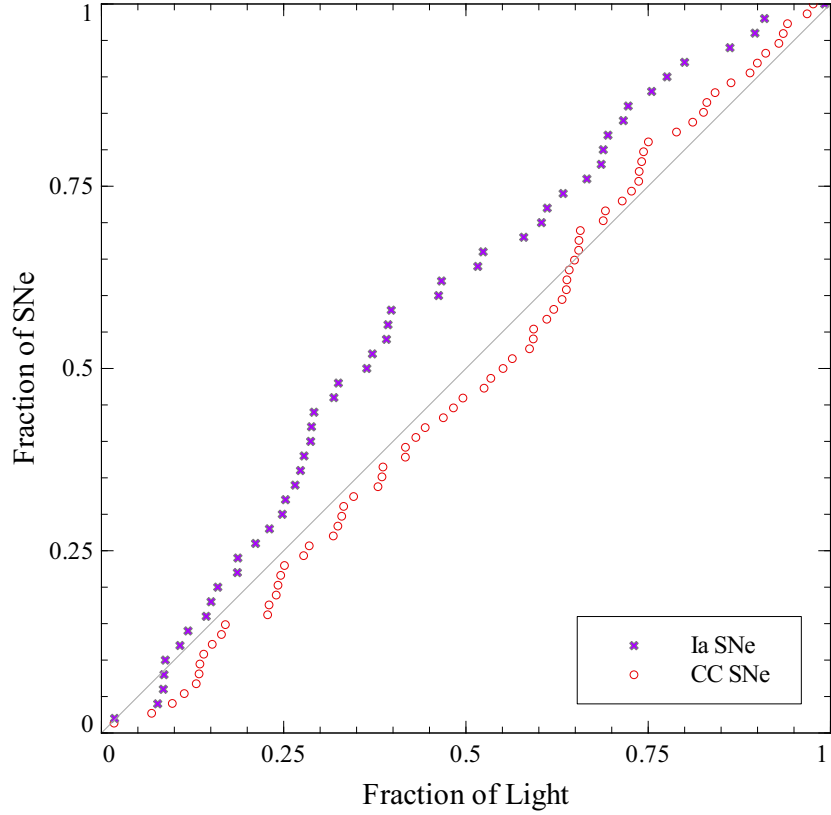
Figure 2.3: A histogram of the number of SNeIa (crosses) located in pixels brighter than a given fraction of the g-band host galaxy light contained within the surrounding "doughnut," which shows that SNeIa tend to occur in dimmer regions. A histogram of SNcc (circles) is also plotted, which closely follows the g-band light distribution. The two supernova histograms are different at the 99.6% confidence level.

2.3   Model Distribution

In such a model, we define the g-band surface brightness at a radius r and angle θ at a given time, t, as the convolution

$$\Sigma_g(r, \theta, t) = \int_0^t dt' L_g(t - t') \dot{\Sigma}(t', r, \theta), \tag{2.2}$$

where $L_g(t)$ is the g-band luminosity per unit solar mass of a population stars with a total age of t and is extracted from a Bruzual & Charlot luminosity model (Bruzual & Charlot 2003; Raskin et al. 2008), and $\dot{\Sigma}(t, r, \theta)$ is the star formation rate surface density as a function of time and position.

13

The star formation rate (SFR) takes the form of a rotating, fixed-body density wave. We approximate the density wave as a Dirac-delta function modulated by a radial profile $\phi(r)$,

$$\dot{\Sigma}(r, \theta, t) = \phi(r) \sum_{n=0}^{\infty} \delta(\theta - n\pi - \Omega_p t), \tag{2.3}$$

where $\dot{\Sigma}$ has units of mass per unit time per unit area, as does ϕ, and Ω_p is the pattern speed of the star-forming density wave in the frame of the stars, whence

$$\Omega_p(r) = \frac{v_0}{r_0}\left(1 - \frac{1}{\sqrt{2}}\right) - \Omega_*(r), \tag{2.4}$$

$$\Omega_*(r) = \begin{cases} v_0/r & r > 1\text{kpc} \\ v_0/1\text{kpc} & r \leq 1\text{kpc}, \end{cases}$$

with v_0 being the circular speed at 1kpc and r_0 is the scale radius. This pattern speed will have a singularity at

$$r = r_0\left(1 - \frac{1}{\sqrt{2}}\right)^{-1} \approx 3.414 r_0, \tag{2.5}$$

where the pattern does not move with respect to the stars. This is called the corotation resonance orbit (Binney & Tremaine 1987; Goldreich & Tremaine 1981) and any simulation would have to terminate at radii below this coordinate.

In our simulations, we used a pattern speed that rotates 2π radians in 300 Myr, although this speed was varied by a factor of two and ruled out as having a significant effect on the results. For calculating Σ_g, the integrated luminosity in the g-band, at some time after the formation of these stars, we employ the stellar evolution data from GALAXEV which gives us the magnitude of a sample of stars at some time t in a particular band. We use the spline routine from numerical methods (Mathews 1992) to construct a semi-analytical expression for the magnitudes with time and convert to a luminosity, L_g, and convolve this expression with the SFR. From this, we obtain an expression for the surface brightness of a pixel (r, θ) at a time t,

$$\Sigma_g(r, \theta, t) = \phi(r) \sum_{n=0}^{\infty} L_g\left(t - \frac{\theta - n\pi}{\Omega_p}\right) |\Omega_p|^{-1}. \tag{2.6}$$

The image created by this simple expression represents a snapshot at a time t of the host galaxy in the g-band.

For modeling the radial profile, observational evidence suggests an exponential in r provides the best approximation, with

$$\phi(r) = \dot{\Sigma}_0 \exp\left(\frac{-r}{r_0}\right), \tag{2.7}$$

14

where $\dot{\Sigma}_0$ sets the star formation amplitude.

In order to compute the SNeIa distribution, we replaced $L_g(t)$ with $SNR_{Ia}(t)$ as given by eq. (2.1), where the prompt component is modeled by a finite-width gaussian distribution of width $\sigma = 0.1\tau$ Myr, centered on an adjustable delay time, τ. Larger values for σ were also attempted, but these did not alter the best-fit τ, and instead only reduced the goodness of fit, with the exception of very large σ values, which yielded poor fits for all τ. Furthermore, it is crucial that the number of prompt and delayed SNeIa in our sample be adjustable rather than just adopting the average low-redshift numbers. This is both becuase our hosts are selected to be star forming, and because of a likely Malmquist bias due to the fact that prompt SNeIa are significantly brighter than delayed SNeIa. Thus we are left with two independent parameters: τ, the delay time, and $F_{delayed}$ the fraction of delayed SNeIa in our sample.

We can estimate this fraction in two ways. First, our SNeIa hosts have a mean color of $B - K = 3.53$. Within this color bin SNeIa occur at roughly three times the rate seen in elliptical galaxies (Mannucci et al. 2005), which would suggest that $F_{delayed} \approx 0.3$. Second, Howell et al. (2007) established a strong correlation between this fraction and the distribution of SNeIa stretches at varying redshifts. They found that long stretches are indicative of prompt SNeIa, while short stretches indicate delayed SNeIa. Figure 2.4 shows a histogram of the stretches for a subset of our sample that are available in the literature (dark gray, Conley et al. 2008) and the distribution for the same redshift bin found by Howell et al. (2007, light gray). Again, because our selection criteria favor star-forming galaxies, a resultant two-component fit using the values for mean stretches ($\bar{s}$) and dispersions (σ) of each component from Howell et al. (2007) demonstrates a mix more heavily favoring the long-stretch, prompt component than would normally be the case in a unbiased sample of low redshift hosts. Integrating these gaussians yields an estimate of $F_{delayed} = 0.56$. For our full analysis then, we consider $F_{delayed}$ to be an adjustable parameter, where our galaxy colors suggest $F_{delayed} \approx 0.3$ and the results of our stretch analysis provide a natural upper limit of $F_{delayed} \leq 0.6$.

For every choice of $F_{delayed}$ and τ, two images were produced and analyzed using the doughnut method: one representing the host surface brightness and the other representing the SNeIa probability density. The radial light decay across the doughnut was also measured for each observed host. For the most part, $\ln[L(r_{SN} - 0.25r_0)] - \ln[L(r_{SN} + 0.25r_0)] \approx 0.5$, where r_{SN} is the radial coordinate of the SN, but a few supernovae were found in regions where this relation

did not strictly hold, and this variation was used as a small modification to our model in a Monte Carlo fashion. However, the model cannot fully account for the numbers of SNeIa observed in pixels fainter than the 20th percentile. In the model galaxy, with a doughnut centered on the annulus containing the SN, the dimmest regions will always lie at the outermost edge of the doughnut where SN probability is zero. In real galaxies, dim regions may lie anywhere, and a small number of the SNeIa will be found in these dim regions.
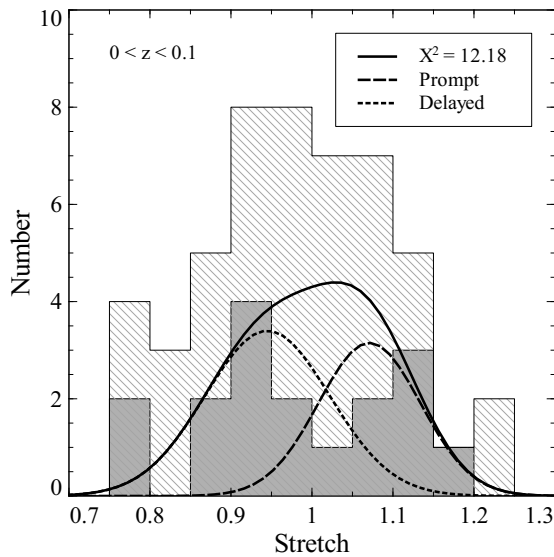
Figure 2.4: A histogram of the distribution of stretches in our sample (dark gray) showing a different distribution as compared to that of Howell et al. (2007) for the same redshift bin (light gray). Using $\bar{s}$ and σ values for each component from Howell et al. (2007), a two-gaussian fit for the prompt and delayed components with $\chi^2 = 12.18$ is overlaid.

For the white dwarf formation rate model (WDFR model), $SNR_{Ia}(t)$ was derived from the Chabrier IMF (Chabrier 2003) convolved with the main-sequence turn-off ages from Bruzual & Charlot (2003) times 10% to approximate stellar lifetimes, for all stars below $8\,M_\odot$ (see Raskin et al. 2008). Stars whose turn-off ages are older than our simulated galaxy ($\approx$10 Gyr) do not contribute to the simulated SN distribution. Pritchet et al. (2008) suggest a uniform conversion of $\sim$1% of all white dwarfs to SNeIa. However, the Fruchter et al. (2006) approach, and by extension our doughnut method, disregards the total count of SNe, instead being concerned only with the relative distribution.

2.4   Results

In Figure 2.5 we plot A+B model distributions with $F_{delayed} = 0.3$ and varying delay times as well as the result of the WDFR model. It is clear from the A+B model curves that larger values

for τ provide increasingly good fits to the data, while the 50 Myr model is inconsistent with the observations. Because our model galaxy has two free parameters, however, we must account for degeneracy between τ and $F_{delayed}$. Figure 2.6 illustrates the two-parameter KS probability map for our sample when compared to our model with varying $F_{delayed}$ values and delay times.
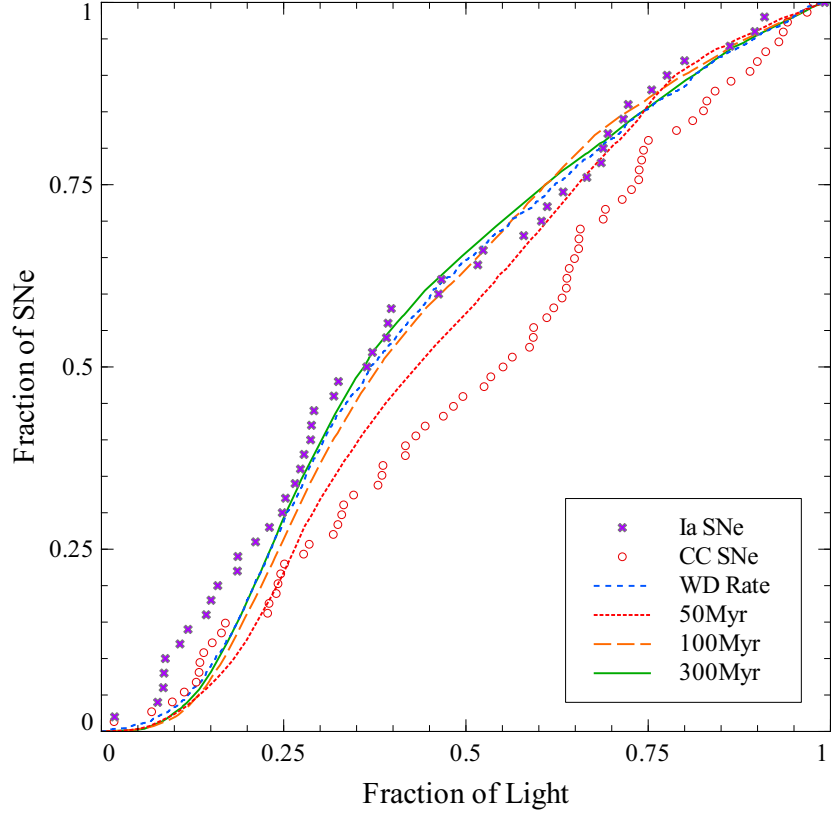
Figure 2.5: Model curves representing the A+B model for several delay times as well as the white dwarf formation rate model are shown compared to the observed distribution of SNeIa. Both the $\tau = 300$ and WDFR models provide excellent fits to the data.

Both the two-parameter map and the average KS probabilities for all tested $F_{delayed}$ values show a clear trend toward longer delay times with the probability reaching its maximum at ≈ 500 Myr and one value of $F_{delayed}$ yielding a probability of 82% at this τ. This is a significant delay time, roughly corresponding to the lifetime of a $2.5\,M_\odot$ star at solar metallicity, and is much longer than the minimum theoretically expected time of 40 Myrs. The best fit delay time for all models, even those with high values of $F_{delayed}$, is longer than 200 Myr and probably longer than 300 Myr. On the other hand, global approaches place an upper limit of $\tau \leq 500$ Myrs (Dahlen et al. 2004; Gal-Yam & Maoz 2004; Mannucci et al. 2005; Scannapieco & Bildsten 2005; Sullivan et al. 2006; Dilday et al. 2008). Relating a 200-500 Myr delay to main sequence

lifetimes, it is clear that majority of SNeIa stars have main-sequence masses less than $3\,M_\odot$, or alternatively, that most SNeIa arise from double-white dwarf binaries. It is important to note that while our model provides strong constraints on the characteristic SNeIa delay time, it does not rule out that a fraction of SNeIa occur at shorter delays (Aubourg et al. 2008; Mannucci et al. 2005; Anderson et al. 2007; Anderson & James 2008; Totani et al. 2008).

In Figure 2.5 we also plot the WDFR, whose similarity to the A+B model with $\tau = 300$ Myrs is striking. One cannot truly be ruled out in favor of the other. A KS test for the WDFR yields a value of 72%, and in fact, the average delay for this model as calculated by $\int_0^\infty SNR(t)tdt / \int_0^\infty SNR(t)dt$ is ≈ 500 Myr.
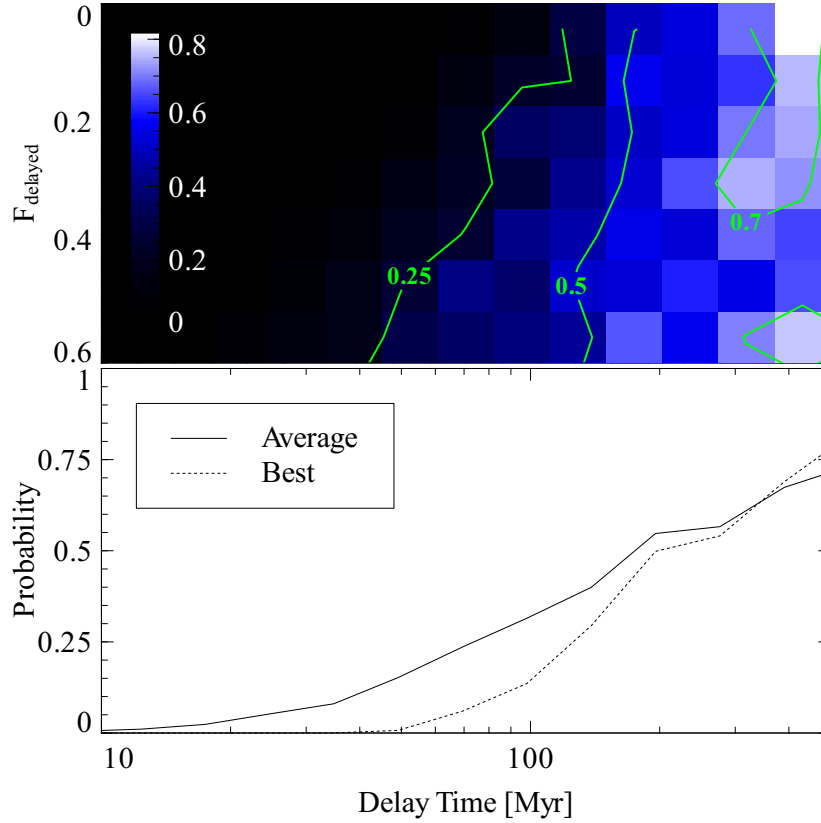
Figure 2.6: Top Panel: A KS probability map for the A+B model with varying parameters $F_{delayed}$ and τ. Degeneracies between the two fit parameters are extremely small. For all values of $F_{delayed}$, $\tau \leq 100$ Myrs is very unlikely, and the best overall fit value is 500 Myrs. The solid contours mark various levels of KS confidence. Bottom Panel: Average and best fit KS probabilities over a range of $F_{delayed}$ values, each as a function of τ, again showing that substantial delay times are highly favored.

Finally, to place an upper limit on the fraction of prompt SNeIa with very short delay times we considered a three-component model in which $SNR(t) = AM_*(t) + B_1\dot{M}_*(t -$

$100 Myrs) + B_2 \dot{M}_*(t - 300 Myrs)$. By fixing τ, we again consider two free parameters, $F_{delayed}$ and B_1/B_{Tot}, the fraction of the prompt component with a delay time of 100 Myrs. For large values of B_1/B_{Tot}, a KS test yields a low statistical likelihood in the model for all values of $F_{delayed}$. We can say with some confidence that the maximum allowed value of B_1/B_{Tot} is 0.3, corresponding to 30% of the prompt component to coming from a 100 Myr old population, while the parameter space with the highest probability has $B_1/B_{Tot} = 0$.

2.5   Discussion

Differentiating the spatial distributions of SNeIa from core-collapse SNe is a difficult problem, both due to the stochastic nature of SNeIa detections and the potential for the delayed component of the Ia rate to obscure the prompt SNeIa spatial distribution. However, by restricting the Fruchter et al. (2006) analysis to an annulus, our "doughnut method" seperates the local host properties from global properties, allowing us to measure the impact of the delay time of the prompt component on the spatial distribution of SNeIa.

By comparing our observations to analytical models, we have established a strong case for a modified A+B model in which the prompt component is delayed by 300-500 Myrs. This long delay time sets important limits on progenitor mechanisms. For the traditional picture of a white dwarf accreting from an evolved, non-degenerate companion, this time delay implies a characteristic companion mass of $\approx 3\,M_\odot$, since stars of this mass evolve on approximately the same time scale. Alternatively, double-degenerate progenitor mechanisms favor long delay times since the time for inspiraling after the formation of the white dwarfs necessarily sets a long minimum time between the formation of stars and SNeIa.

Note that the time delay derived here is an average time and that there can be a considerable spread in this value. Thus, a three-component model allows up to 30% of the prompt component to have shorter delay times ≈ 100 Myrs, as suggested by Auborg et al. (2008) and Mannucci et al. (2006). We also found that a model in which the Ia rate is directly proportional to the white-dwarf formation rate, as considered by Pritchet, Howell & Sullivan (2008), reproduces the observed spatial distributions of SNeIa very well.

Regardless of which model proves to be the best fit, it is this characteristic timescale that is most important for calculations of cosmic enrichment, and the results of our analysis using both the A+B model and the WDFR model are evidence of a long characteristic timescale.

One caveat is that all our measurements have been made in relatively high-metallicity grand-design sprial galaxies, and several observational and theoretical studies have hinted that SNeIa rates and properties may be substantially different at lower metallicities (Timmes et al. 2003; Gallagher et al. 2008; Cooper et al. 2009). There is still much more to be learned about these ubiquitous but mysterious cosmological probes.

^{56}Ni PRODUCTION IN WHITE DWARF COLLISIONS

In this chapter, beginning the series on numerical studies of progenitor mechanisms, we present a comprehensive study of white dwarf collisions as an avenue for creating type Ia supernovae. Using a smooth particle hydrodynamics code with a 13-isotope, α-chain nuclear network, we examine the resulting ^{56}Ni yield as a function of total mass, mass ratio, and impact parameter. We show that several combinations of white dwarf masses and impact parameters are able to produce sufficient quantities of ^{56}Ni to be observable at cosmological distances. We find the ^{56}Ni production in double-degenerate white dwarf collisions ranges from sub-luminous to the super-luminous, depending on the parameters of the collision. For all mass pairs, collisions with small impact parameters have the highest likelihood of detonating, but ^{56}Ni production is insensitive to this parameter in high-mass combinations, which significantly increases their likelihood of detection. We also find that the ^{56}Ni dependence on total mass and mass ratio is not linear, with larger mass primaries producing disproportionately more ^{56}Ni than their lower mass secondary counterparts, and symmetric pairs of masses producing more ^{56}Ni than asymmetric pairs.

3.1   Introduction

While the preferred mechanism for type Ia supernovae involves a single white dwarf star accreting material from a non-degenerate companion (Whelan & Iben 1973; Nomoto 1982; Hillebrandt & Niemeyer 2000), recent observational evidence suggests a non-negligible fraction of observed SNeIa may derive from double-degenerate progenitor scenarios. Scalzo et al. (2010) observed the supernova SN 2007if photometrically, and assuming no host galaxy extinction, they found $1.6\pm0.1\,M_\odot$ of ^{56}Ni with 0.3-0.5 $M_\odot$ of unburned carbon and oxygen forming an envelope. This ^{56}Ni yield implies a progenitor mass of $2.4\pm0.2\,M_\odot$, which is well above the Chandrasekhar limit - the maximum mass for a non-rotating white dwarf (Chandrasekhar 1931, Pfannes et al. 2010, Yoon & Langer 2004, Yoon & Langer 2005). It follows that two white dwarfs must have been involved in the event that produced SN 2007if, since a single white dwarf cannot accrete enough material to reach this mass without either exploding as a SNIa or collapsing to form a neutron star (Yoon et al. 2007). Furthermore, spectroscopic observations by Tanaka et al. (2010) suggest SN 2009dc produced $\gtrsim 1.2\,M_\odot$ of ^{56}Ni, depending on the assumed dust absorption. This also

implies a progenitor mass $> 1.4\,M_\odot$ as $0.92\,M_\odot$ of ^{56}Ni is the greatest yield a Chandrasekhar mass can produce (Khokhlov et al. 1993).

Howell et al. (2006) inferred from their observations of SN 2003fg that $\sim 1.3\,M_\odot$ of ^{56}Ni was produced, as did Hicken et al. (2007) in their observations of SN 2006gz. There is a growing body of evidence supporting double-degenerate SNeIa progenitor systems. Since any supernova arising from a double-degenerate progenitor scenario may not fit the standard templates for SNeIa, these transients must be filtered out if SNeIa are to remain as premier cosmological tools. To that end, we must develop models that give clear and detectable signatures of double-degenerate SNeIa to distinguish them from standard SNeIa.

Currently, models of double-degenerate progenitors are split into two, dynamically different scenarios. In the first, white dwarfs in close binaries lose angular momenta through gravitational radiation, ultimately merging into a thermally supported super-Chandrasekhar object or detonating outright (Iben & Tutukov 1984; Webbink 1984; Benz et al. 1989a; Yoon et al. 2007; Pakmor et al. 2010). In the second, two white dwarfs collide in dense stellar systems such as globular cluster cores (Raskin et al. 2009; Rosswog et al. 2009; LorŐn-Aguilar et al. 2009; LorŐn-Aguilar et al. 2010), where white dwarf number densities can be as high as $\approx 10^4$ pc^{-3}. This follows from conservative estimates for the average globular cluster mass, $10^6\,M_\odot$ (Brodie & Strader 2006), and for an average globular cluster core radius, 1.5 pc (Peterson & King 1975), taken together with the Salpeter IMF (Salpeter 1955). Assuming cluster velocity dispersions on the order of 10 km s^{-1}, this allows for $10 - 100$, $z \lesssim 1$ collisions per year. Observations by Chomiuk et al. (2008) of globular clusters in the nearby S0 galaxy NGC 7457 have detected what is likely to be a SNIa remnant. Given the difficulty in distinguishing SNeIa as residing in galaxy field stars or in globular clusters in front of or behind their host galaxies (Pfahl et al. 2009), the frequency with which these can occur warrants investigation.

Numerical simulations of white dwarf collisions were pioneered in Benz et al. (1989b) using a smooth particle hydrodynamics (SPH) code. They concluded from their results that white dwarf collisions were of little interest as the ^{56}Ni yields were small. However, their simulations employed an approximate equation of state for white dwarfs and resolutions were low, relative to what is possible with current computing resources. Moreover, as will be discussed, the infall velocities and velocity gradients play a crucial role in the final ^{56}Ni yields.

More recently, Raskin et al. (2009), Rosswog et al. (2009), and LorŐn-Aguilar et al. (2010)

revisited collisions using up-to-date SPH codes and vastly more particles (8×10^5, 2×10^6, and 4×10^5, respectively). In Raskin et al. (2009), a single mass pair ($0.6\,M_\odot \times 2$) was explored with three impact parameters, whereas in Rosswog et al. (2009), several mass pairs were examined in direct, head-on collisions. Both of these papers aimed at establishing double-degenerate collisions as SNeIa progenitors, finding that ^{56}Ni is indeed produced prodigiously in such collisions, lending credence to their candidacy. LorŐn-Aguilar et al. (2010) examined one mass pair ($0.6\,M_\odot + 0.8\,M_\odot$), but at a number of different impact parameters, ranging from those that resulted in direct collisions to those that resulted in eccentric binaries, aimed at establishing the parameters of white dwarf coalescence arising from collisional dynamics.

In this chapter, we revisit the three impact parameters studied in Raskin et al. (2009) using a variety of mass pairings. Using 22 combinations of masses and impact parameters, we aim to answer five key questions; how does ^{56}Ni production depend on

- the total mass of the system?

- the mass ratio of the two stars?

- the impact parameter?

- the infall velocities of the constituent stars?

- tidal effects?

While the last two of these questions can be eliminated with robust initial conditions, they are nevertheless important details that are sometimes overlooked. Armed with this information, we will be able to make some conclusions about the observability of different combinations of collision parameters, and to determine whether the resulting transient of any particular collision is as luminous as a SNIa.

The structure of this chapter is as follows. In §2, we discuss the details of our initial conditions and our new hybrid burning nuclear network. In §3, we give the details of the results of each simulation that resulted in a detonation along with a study of the effect of numerical parameters on the ^{56}Ni yield in §3.1.2, and in §4, we discuss those that resulted in remnants. Finally, in §5, we summarize our results and conclusions.

3.2 Method
Particle Setups & Initial Conditions

As in Raskin et al. (2009), we employ a version of a 3D SPH code called SNSPH (Fryer et al. 2006). SPH codes are particularly well suited to these kinds of simulations as the white dwarf stars involved are very dense and moving very rapidly. Advecting rapidly moving, isothermal, cold white dwarfs in Eulerian, grid-based codes introduces perturbations that can be challenging to overcome. Moreover, because many of our simulations are grazing impacts, conservation of angular momentum is crucial to the final outcomes, for which SNSPH excels (Fryer et al. 2006).

We used a Weighted Voronoi Tessellations method (WVT, Diehl & Statler 2006) for our particle setups. This method arranges particles in a pseudo-random spatial distribution with thermodynamic quantities that are consistent with the chosen equation of state (EOS). The default operation for this method is to allow the masses of particles to vary in order to keep their sizes, or smoothing lengths (h), constant throughout the initial setup. This approach has its advantages when it comes to spatial arrangement, but one disadvantage is that it produces a uniform level of refinement in the initial conditions regardless of where most of the mass resides. The result is that much higher particle counts are required to reach convergence.

To remedy this, we modified the WVT method to keep mass fixed, varying h consistent with the density profiles of white dwarf stars. This has the effect of concentrating resolution where most of the mass resides, vastly reducing the required particle counts for convergence. In fact, whereas in Raskin et al. (2009), we showed that convergence of the ^{56}Ni yield was reached at approximately 10^6 particles, using constant mass particles, we reach convergence with only 200,000. A convergence test on particle count of our fiducial case, $0.64\,M_\odot \times 2$ with zero impact parameter, is discussed in §3.1.2.

A further modification we have added to our previous approach is an isothermalization step in our initial conditions. When mapping 1D profiles for cold white dwarfs onto a resolution limited, 3D particle setup, there is often a relaxation time, during which the stars oscillate before finding equilibrium. For white dwarf masses of $\approx 0.6\,M_\odot$, this settling time is short, but for larger masses, the oscillations can continue for several minutes or hours. These repeated gravitational contractions heat the interiors of the stars until they can no longer be considered "cold" white dwarfs. Therefore, we relaxed each individual star in a modified version of SNSPH

that artificially cools the stars by keeping each particle at a constant temperature during the stars' oscillations until they reach a cold equilibrium. Figure 3.1 shows a temperature profile for a $0.64\,M_\odot$ white dwarf that has been passed through this isothermalization routine, indicating an isothermal temperature of $\approx 10^7$K throughout.
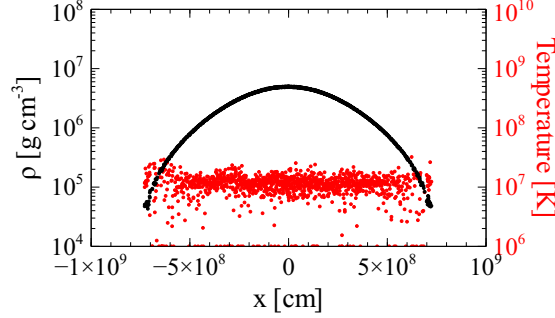
Figure 3.1: Temperatures and densities of particles lying on the x-axis in a $0.64\,M_\odot$ white dwarf. This star was created using WVT and isothermalized to 10^7K after ~ 5 minutes.

As in our previous work, the initial conditions for the positions and velocities of the white dwarf stars in our simulations were generated using a fourth-order Runge-Kutta solver with an adaptive time-step that integrates simple kinematic equations. The impactor star was initially given a small velocity comparable to the velocity dispersion of globular cluster cores, $\sigma = 10$km/s. The solver places the stars at $0.1\mathrm{R}_\odot$ apart with the proper velocity vectors expected for free-fall from large initial separations with a given velocity dispersion.

Figure 3.2 compares the initial conditions of the $0.64\,M_\odot \times 2$, head-on collision to the velocity gradient that is introduced by tidal forces. The relative velocity of the centers of mass can be predicted analytically for a zero impact parameter collision with $v_c = [2G(M_1 + M_2)/\Delta r]^{1/2}$, where M_i are the masses of the constituent white dwarfs and Δr is the separation of their centers of mass.

As Figure 3.2 demonstrates, when the stars are allowed to free-fall in SNSPH from larger separations, such as the separation of $0.1\mathrm{R}_\odot$ used throughout this paper, the velocity gradients that arise from tidal distortions are non-negligible. As will be shown in §3.1.2, the magnitudes of these velocities and their spreads play an important role in the final outcomes and the ^{56}Ni yields of each simulation as they determine how much kinetic energy is converted to thermal energy, and thusly, when carbon-ignition occurs. A shooting-method was used to determine the necessary, initial vertical separation that resulted in the final impact parameter that we desired
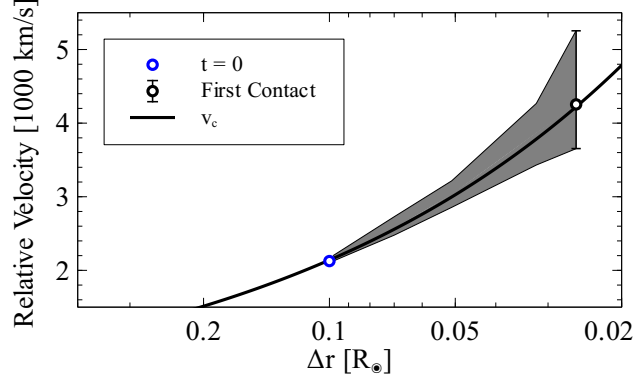
Figure 3.2: The velocity evolution from our initial conditions to the moment of first contact, indicating strong velocity gradients induced by tidal forces. The shaded area denotes the spread in relative x-velocities, and v_c is the relative velocity of the centers of mass.

at the moment of impact. Initial velocities for all of our collision scenarios with zero impact parameter are given in Table 3.1.

Table 3.1: Initial velocities of each component star in the head-on cases of each mass pair for initial separations of $0.1 R_\odot$. All velocities are relative to the center of mass.

#	m_1 [$M_\odot$]	m_2 [$M_\odot$]	$-v_1$ [$\times 10^3$km/s]	v_2 [$\times 10^3$km/s]
1	0.64	0.64	1.10	1.10
2	0.64	0.81	1.31	1.03
3	0.64	1.06	1.58	0.95
4	0.81	0.81	1.24	1.24
5	0.81	1.06	1.51	1.15
6	0.96	0.96	1.35	1.35
7	1.06	1.06	1.41	1.41
8	0.50	0.50	0.97	0.97

Likewise, all of our stars are initialized with 50% ^{12}C and 50% ^{16}O throughout. This approximates typical carbon-oxygen white dwarf compositions, and we use the Helmholtz free-energy EOS (Timmes & Arnett 1999; Timmes & Swesty 2000).

Hybrid Burner

Most large, hydrodynamic codes use some form of a hydrostatic nuclear network (e.g. Eggleton 1971; Weaver et al. 1978; Arnett 1994; Fryxell et al. 2000; Starrfield et al. 2000; Herwig 2004; Young & Arnett 2005; Nonaka et al. 2008). That is, the thermodynamic conditions present at the start of a burn calculation are not altered until the next hydrodynamic time step, which often times is controlled by abundance or energy changes from the burn calculation rather than a pure Courant condition. The effect of this is to fix the temperature-dependent reaction rates

throughout the hydrodynamic time step to what they were at its start.

There are several reasons for running a simulation this way, the most important of which is to avoid a decoupling of the nuclear network from the hydrodynamic calculation. However, for limited spatial, mass and time resolutions, this approximation - that the thermodynamic conditions do not change rapidly enough during a burn to warrant a sub-cycle recalculation of the nuclear reaction rates - fails in regimes where the nuclear reactions are strongly temperature dependent, such as at temperatures where photo-disintegration is the dominant nuclear process. As Figure 3.3 shows below, the nuclear statistical equilibrium (NSE) state for material with $\rho = 1 \times 10^6$ g cm^{-3} at $T_9 \approx 7$ has most of the heavy isotopes photo-disintegrating back to ^{4}He.
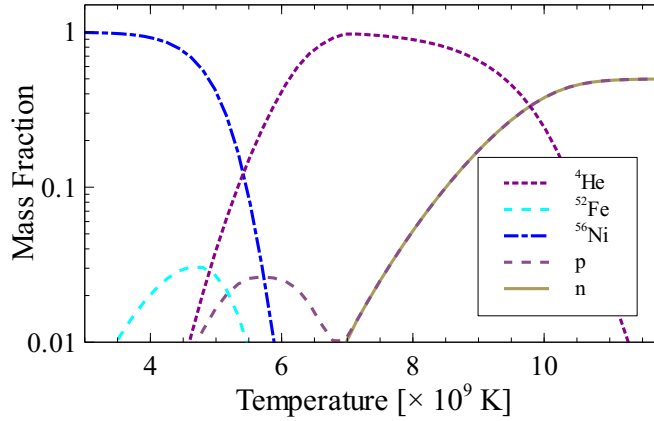
Figure 3.3: NSE distributions for ρ =1e7 g cm^{-3} and Y$_e$=0.5 in an α-centric nuclear network. Proton and neutron mass fractions are plotted for reference. At $T_9 \approx 6$, ^{4}He begins to dominate the isotope distribution.

In such a regime, the material undergoing photo-disintegration experiences what amounts to an abrupt phase change through a strongly endothermic reaction. In nature, this reaction should rapidly cool the material before complete photo-disintegration, allowing these liberated α-particles to react with other isotopes. However, a hydrostatic burn will overestimate the time-scale for this cooling as it assumes a full hydrodynamic time step is necessary for relevant pressure or temperature changes. With the temperature remaining fixed over an artificially long time, this approach results in the nuclear network removing far too much internal energy, u, to be physical.

Typically, one attempts to limit the impact of such a phase change by relying on a

27

global time-step minimization scheme of the form

$$\Delta t_{n+1} = \min \left[\Delta t_c, \Delta t_n \times f_u \times \left(\frac{u_{n-1}^i}{u_n^i - u_{n-1}^i} \right) \right],$$ (3.1)

where the subscript n refers to the iteration number, Δt_c is the Courant time, u^i is the specific internal energy of the ith particle, and f_u is a dimensionless parameter which constrains the maximum allowable change in energy. Our global time-step is also controlled in this manner. In practice, the conditions immediately prior to photo-disintegration will fix the next time-step, Δt_{n+1}, to of order 10^{-5}s for $f_u = 0.30$. However, even this time-step is too large to capture the relevant temperature changes effecting the reaction rates on time-scales of order 10^{-12}s.

The alternative approach to a hydrostatic burn is to use a "self-heating/cooling" nuclear network that simultaneously integrates an energy equation and the abundance equation self-consistently (see e.g. Müller 1986). When applied to a particle code like SPH, this type of calculation keeps ρ fixed, but updates temperature in a fashion that is consistent with the equation of state and the new internal energy at each sub-cycle.

The ordinary differential equation that governs a hydrostatic burn calculation of the abundance of an isotope Y_i, assuming the mass diffusion gradients are negligible, is of the form

$$\begin{aligned} \dot{Y}_i &= \sum_j C_i R_j Y_j \\ &+ \sum_{j,k} \frac{C_i}{C_j! C_k!} \rho N_A R_{j,k} Y_j Y_k \\ &+ \sum_{j,k,l} \frac{C_i}{C_j! C_k! C_l!} \rho^2 N_A^2 R_{j,k,l} Y_j Y_k Y_l, \end{aligned}$$ (3.2)

where the coefficients $C_{i..l}$ specify how many particles of the ith species are created or destroyed, and $R_{i..l}$ are the temperature-dependent reaction rates for each of the different reaction types. The first term describes weak reactions (β-decays and electron captures) and photo-disintegrations, the second describes two-body reactions of the type ^{12}C$(\alpha,\gamma)^{16}$O, and the third term describes three-body reactions, such as ^{4}He$(2\alpha,\gamma)^{12}$C. The energy generation ODE takes the form

$$\dot{\epsilon} = -N_A \sum_i \dot{Y}_i m_i c^2,$$ (3.3)

where m_i is the rest-mass of the ith isotope (see e.g. Benz et al. 1989b). The density and temperature equations are simply $\dot{\rho} = 0$ and $\dot{T} = 0$, respectively, in a hydrostatic burn.

A self-heating at constant density calculation modifies only the temperature equation, starting from the first law of thermodynamics in specific mass units,

$$\frac{du}{dt} - \frac{P}{\rho^2}\frac{d\rho}{dt} = T\frac{ds}{dt}, \tag{3.4}$$

where du/dt is the change in specific energy and ds/dt is the change in specific entropy. In accordance with $\dot{\rho} = 0$ and employing the identity $T\dot{s} = \dot{\epsilon}$, this reduces to

$$\frac{\partial u}{\partial T}\frac{dT}{dt} = \dot{\epsilon}$$
$$\dot{T} = \frac{\dot{\epsilon}}{c_v}, \tag{3.5}$$

where c_v is the specific heat capacity at a constant volume. Equations (3.2), (3.3), and (3.5) are evolved simultaneously and self-consistently (Müller 1986).

At very high spatial resolutions and small time-steps, the self-heating approach would be identical to the hydrostatic approach. As Figure 3.4 shows for the energy, temperature and composition of a single particle over a finite and relatively large time-step as determined by Equation (3.1) with $f_u = 0.30$, these two burning calculations reach very different conclusions about the final energy and composition of the particle after photo-disintegration.

To capture the relevant temperature changes using a hydrostatic approach would require a global time-step $\sim 10^{-12}$s, where the temperatures of the two calculations have diverged by $\approx 5\%$. This is problematic for two reasons: 1) such a time-step cannot be predicted from the conditions immediately prior to photo-disintegration, and 2) having such a small global time-step exceeds the limit of machine precision for many hydrodynamic codes, SNSPH included. When SNSPH attempts to calculate velocities for the next time-step using $\Delta t \sim 10^{-12}$s, it often fails or returns zero.

Unfortunately, a self-heating nuclear network can also expose the weakness of a mass resolution limit. For a typical simulation of 10^6 particles, each particle has a mass of $\approx 10^{27}$g. A self-heating nuclear calculation for carbon-burning of such large masses becomes rapidly explosive on time-scales approaching the Courant limit. Without any mechanism for energy transport on such short time-scales, the assumption of a homogeneous burn of all 10^{27}g begins to break down. The vigorous burning of so much material rapidly liberates more energy than the binding energy of the star.

Our "middle-path" solution to these two extremes is a hybrid-burning scheme wherein a combination of these two approaches is used under different circumstances. Since the hydrostatic
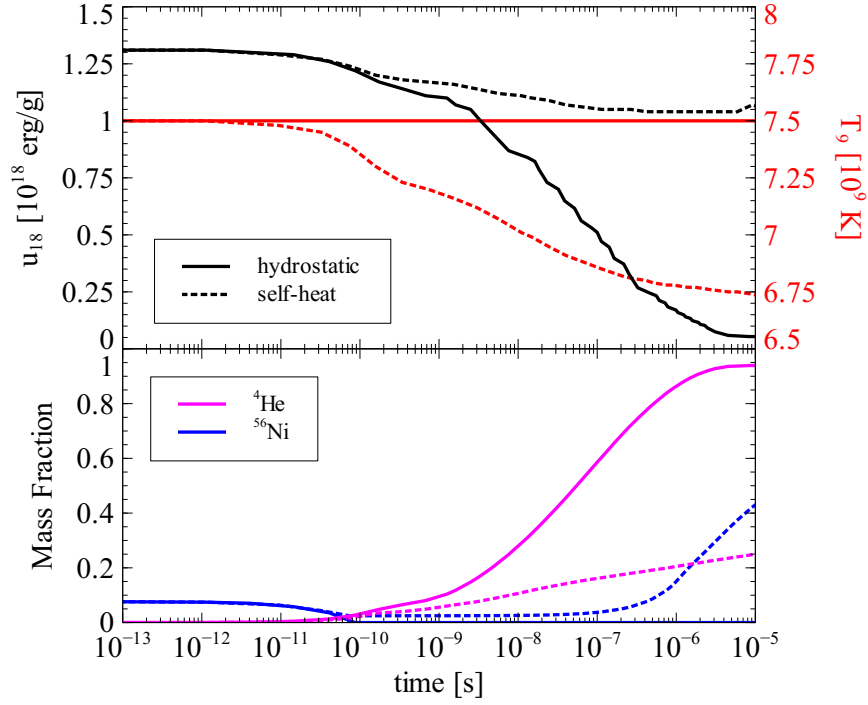
Figure 3.4: Calculations of the energy, temperature, and composition of a particle after a representative time-step as determined by Equation (3.1) with $f_u = 0.30$. Solid lines show the implicit integrations from a hydrostatic calculation, while dotted lines indicate those for a self-heating calculation. In both cases, ρ is kept constant, while in the self-heat calculation, the temperature, and thus the nuclear reaction rates, are recalculated at each implicit integration step, consistent with the first law of thermodynamics.

approach is a better approximation for exothermic reactions at our resolution limit, the self-heating/cooling approach is only employed for particles that undergo strong, net endothermic reactions such as photo-disintegration. This allows these particles to smoothly "step over" the photo-disintegration phase change without artificially losing too much energy. We apply this approach, along with the time-step minimization of Equation (3.1), to the α-chain aprox13 nuclear network (Timmes 1999; Timmes et al. 2000) by imposing the condition that if $\dot{\epsilon} < 0$ after a hydrostatic burn, the burn is recalculated employing Equation (3.5).

While stepping through a photo-disintegration process is an interesting wrinkle for numerical simulations of double-degenerate white dwarf collisions, it is not a significant factor for ^{56}Ni production. In all of our simulated cases, we found that on average $< 2\%$ of particles experienced this phase change. For the most part, the local conditions for a number of particles wherein a single particle might undergo photo-disintegration are sufficiently high-energy that the neighboring particles will have already initiated a detonation. Based on the results

of our simulations, we do not expect that collisions with yet higher kinetic energies than those attempted here would paradoxically yield less ^{56}Ni due to photo-disintegration effects.

3.3 Results & Analysis I - Detonations

Our previous work narrowed the range of pertinent impact parameters to three scenarios, which we revisited for each of our mass combinations. We simulated head-on impacts, partially grazing collisional impacts, and fully grazing/glancing impacts. Table 3.2 summarizes the ^{56}Ni yields of each of our simulations. In this table, the impact parameter, b (the vertical separation between the cores of both white dwarfs at the moment of impact) is given as the fraction of the radius of the primary white dwarf. Thus the $b = 0$ column shows the yields for head-on impacts, the $b = 1$ column indicates a full white dwarf radius and $b = 2$ indicates 2 white dwarf radii, or a fully grazing impact.

Table 3.2: Simulation ^{56}Ni yields for various mass combinations and parameters. Values indicated with a ($\square$) are those simulations that resulted in remnants. Dashes (–) indicate combinations of parameters we did not simulate. All simulations listed here used $f_u = 0.30$ and 200k particles.

#	$m_1\ [M_\odot]$	$m_2\ [M_\odot]$	$m_{tot}[M_\odot]$	$b = 0$	$b = 1$	$b = 2$
1	0.64	0.64	1.28	0.51	0.47	$\square$
2	0.64	0.81	1.45	0.14	0.53	$\square$
3	0.64	1.06	1.70	0.26	$\square$	$\square$
4	0.81	0.81	1.62	0.84	0.84	0.65
5	0.81	1.06	1.87	0.90	1.13	$\square$
6	0.96	0.96	1.92	1.27	1.32	1.33
7	1.06	1.06	2.12	1.71	1.72	1.61
8	0.50	0.50	1.00	0.00	–	–

Dursi & Timmes (2006) examined the shock-ignited detonation criteria for carbon in a white dwarf using numerical models. They derived a relationship between the density of the carbon fuel and the minimum radius of a burning region that will launch a detonation. For a carbon abundance of $X_{^{12}C} = 0.5$ and densities typically found in the white dwarfs used in our simulations, $\rho \sim 10^7 \mathrm{g\ cm}^{-3}$, their results suggest a minimum burning region, or match head size of $r_b \sim 10^4$cm. This is three orders of magnitude smaller than our smallest particle size, and properly resolving this criterion would require $\sim 10^{12}$ particles. Such a high-resolution study is too expensive with our current computing resources, and therefore, we acknowledge that we cannot resolve the precise detonation mechanism in our simulations.

The criteria established in Dursi & Timmes (2006) would suggest that a single particle

in any of our simulations can initiate a detonation. However, in order for a detonation to be sustained, the energy that the initiating particle deposits in its neighbors must be sufficient to cause those neighbors to liberate an equal amount of nuclear energy. This somewhat softens the ability of a single particle to initiate a sustainted detonation. Indeed, in all of our simulations, we found that several particles ignited nearly simultaneously, or at least outside of causal contact with one another in order to initiate a sustained detonation. Moreover, the pressure gradient established by particles neighboring those that reached ignition needed to be favorable for a significant and rapid energy deposition.

In SPH, energy is shared between particles via PdV work with

$$\dot{u}_{ij} = \frac{P_i}{\rho_i^2} m_j \Delta v_{ij} \cdot \nabla_i W_{ij}, \tag{3.6}$$

where P_i and ρ_i are the pressure and density of particle i, m_j is the mass of particle j, Δv_{ij} is the difference in velocities of particles i and j, and W_{ij} is the SPH smoothing kernel. For each particle i, there is an implied sum over all particles j. In SPH formalism, the condition for a sustained detonation would require that this quantity is large enough to ignite explosive burning in particle i. Put another way, if particle i generates energy ϵ_i at time t_0, $\dot{u}_{ji}$ must be sufficient such that at time $t_0 + \Delta t$, $\dot{\epsilon}_j \approx \dot{\epsilon}_i$, where Δt is the Courant time. This requires a proportionality between the energy generation rate in particle i and the pressure gradient with its nearest neighbors, and to first order, this criterion reduces to

$$\dot{\epsilon}_i \geq \frac{P_i}{c_s \rho_i^2} \nabla P_{ij}. \tag{3.7}$$

For a given energy generation rate, large and positive pressure gradients can inhibit a detonation breakout. In situations where particles ignited carbon-burning, but were nevertheless unable to deposit enough energy into their neighbors to cause them to also ignite, the material settled into a slow-burn regime rather than detonating. While we cannot resolve the detonation mechanism to the desired precision, we compared one-dimensional ZND detonation profiles (see e.g. Fickett & Davis 1979) with detonation profiles from one-dimensional slices through the SNSPH models and concluded that our collision calculations are resolving the detonation widths and structures to within 20%.

Mass Pair 1 - 0.64 $M_\odot$ × 2

Fiducial Case

We recalculated the $\approx 0.6\,M_\odot$ equal mass case as in Raskin et al. (2009) to establish a baseline comparison with our equal-mass particle configuration and hybrid-burner technique. Empirical white dwarf mass functions (e.g. , Williams, Bolte, & Koester 2004) suggest collisions with this mass pair are expected to be among the most common. With our equal-mass particle constraint, the final mass of the star used in the simulations came to $0.64\,M_\odot$.

The right-top panel of Figure 3.5 shows that when the stars first collide the infall speeds, v_x of material entering the shocked region are greater than the sounds speeds, c_s, resulting in a stalled shock in that region. The conditions in the center plane of this shocked region (the y-z plane, $\rho \approx 10^{6.5-7}$ g cm^{-3} and $T_9 \approx 1$) are sufficient to ignite carbon with an energy-generation rate scaling roughly as $\dot\epsilon \sim \rho T^{22}$, burning up to silicon at $T_9 \approx 3$. The separation of material into three distinct phases is clearest in the left two panels of Figure 3.5, which plots particle number density in the ρ-T plane. The lower, more populated region is unshocked, carbon-oxygen material and is indicated in green. The less populated middle region, also represented with green at $T_9 \approx 1$, is shocked material that has yet to reach the critical conditions for carbon ignition, and the upper, sparse region is material that has begun burning carbon to silicon-group elements, represented in red.

The pressure gradient slopes positively in all directions away from the geometric center where this early burning begins, which is in fact at lower densities than the surrounding shocked medium. While the whole of the shocked region continues to heat up, causing more material to ignite near the center, the steep pressure gradient prevents the energy liberated by burning to initiate a detonation. For these burning particles, with silicon ash behind them and higher pressure carbon in front, the energy they deposit in their neighbors is insufficient to greatly alter their energy-generation rate. Instead, the burning region grows only as fast as material is heated to the critical temperatures needed for carbon ignition, $T_9 \approx 1$, by the conversion of kinetic energy to thermal energy.

Approximately two seconds after the stars first collide, sufficiently high temperatures and densities are reached at the edges of the shocked region to initiate carbon-burning. In these locations, the pressure gradient slopes negatively in all directions. The liberated energy is free

33
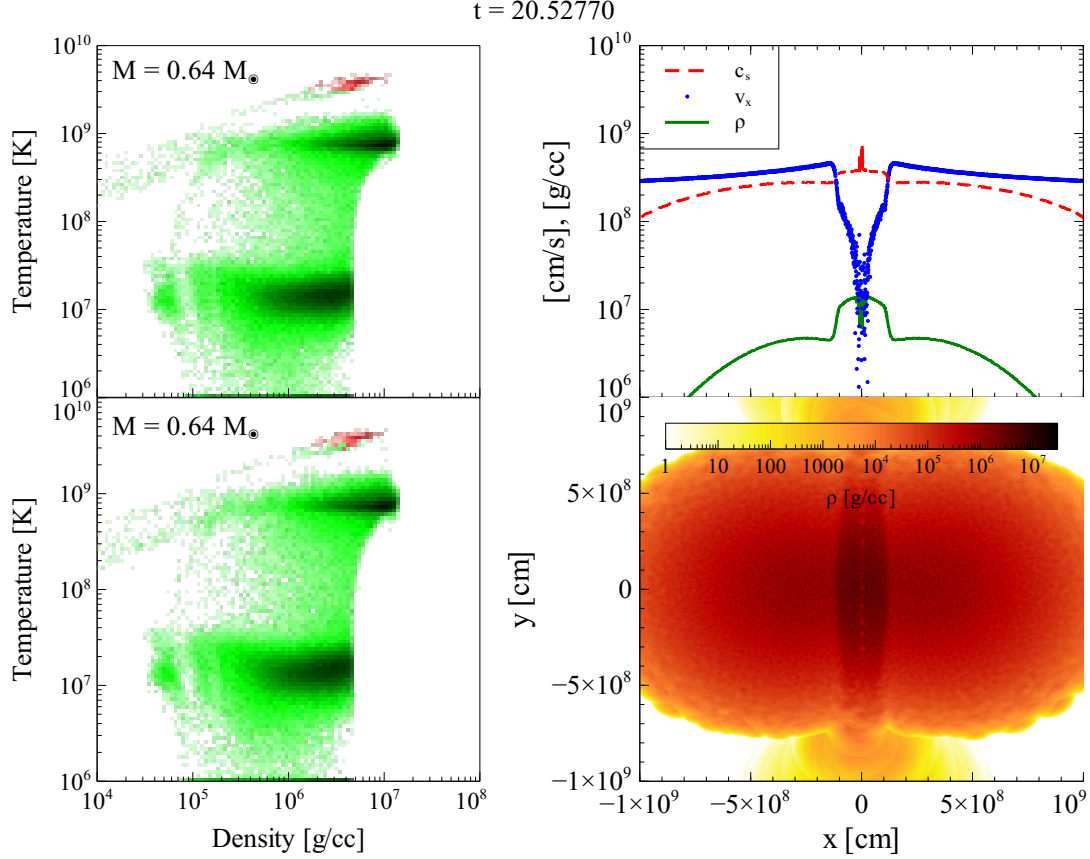
Figure 3.5: Left Panels: Density vs. temperature for all particles from each constituent star in mass pair 1, $0.64\,M_\odot \times 2$ and $b = 0$. Each point is colored indicating the isotope(s) with the greatest abundance and by the particle number density at each $\rho - T$ coordinate. Green indicates high concentrations of carbon and oxygen, red indicates silicon group elements, and blue indicates iron-peak elements, most predominantly ^{56}Ni. The darker the color in each group, the higher the particle number density. Right-top Panel: Sound speed, infall velocity, and density for particles lying on the x-axis. Right-bottom Panel: A slice in the x-y plane of particle densities.

to break out, initiating detonations at the ignition points. The sound speeds in these zones are raised higher than the infall speeds due to the rapid rise in temperature, and ^{56}Ni begins to appear in large quantities, indicated in blue in the left panels of Figure 3.6.

Sustained detonation fronts then propagate through the unburned material, as well as the silicon "ash" that lies in the shocked region. As Figure 3.7 shows, significantly more ^{56}Ni is produced during this phase. In Figure 3.7, it is also evident that the shocks overtake one another inside the contact zone, shocking the material a second time and producing yet more ^{56}Ni. Less than one second after the detonations began, the entire system has become unbound, freezing out the nuclear reactions, as can be seen in Figure 3.8. The final ^{56}Ni yield for this
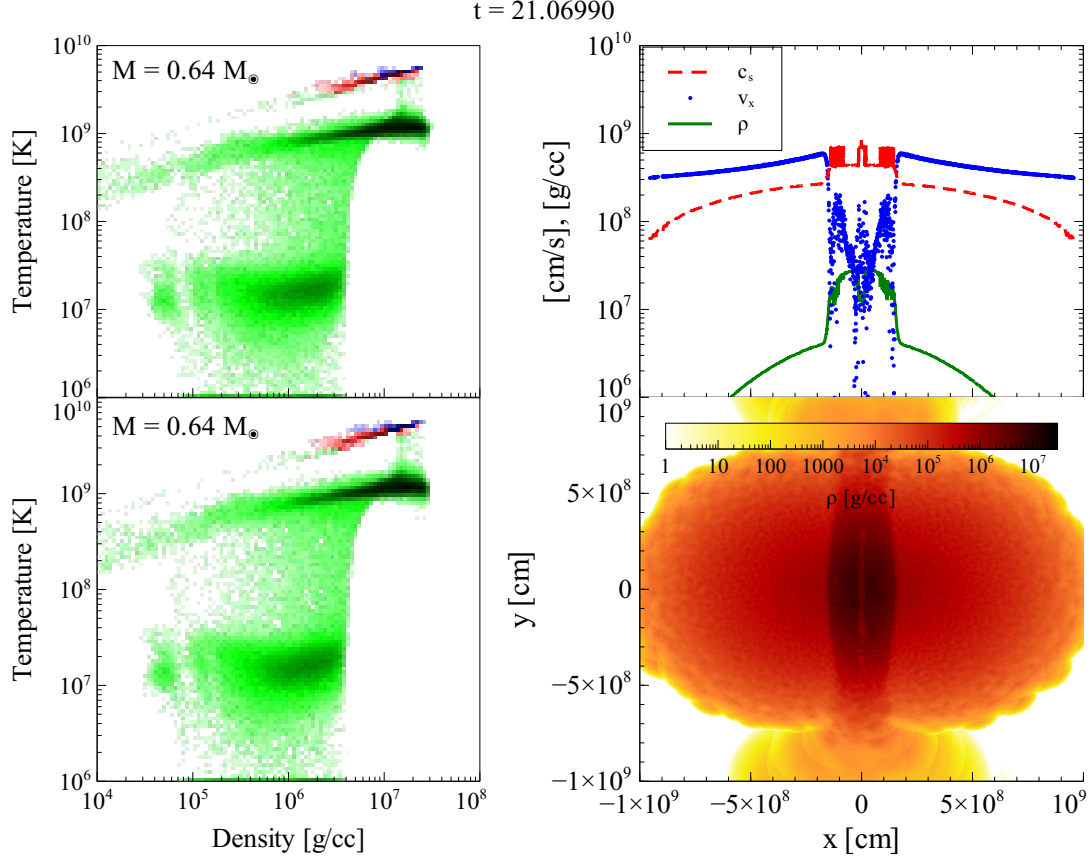
Figure 3.6: Same format as Figure 3.5, at a later time in the simulation.

simulation was $0.51\,M_\odot$.

In the $b = 1$ simulation, the added angular momentum distorted the shocked region between the two stars, resulting in detonations lighting off-center and off-axis as compared to the $b = 0$ case. As Figure 3.9 shows, the detonation waves traveling through the densest portions of the shocked regions where the sound speed is highest, twist the material into a uniquely anisotropic configuration. Moreover, because much of the material is traveling nearly perpendicular to the shock, the density in the pre-detonation, shocked region is lower than in the $b = 0$ case. This reduces ^{56}Ni production by about 7% to $0.47\,M_\odot$.

Since the post-explosion, expansion phase is homologous, the pattern of isotopes present at the moment the system becomes unbound is not altered by the expansion. Therefore, the velocities plotted in Figure 3.10 for several isotopes in the $b = 0$ and $b = 1$ cases are directly related to the radial distribution of the isotopes.
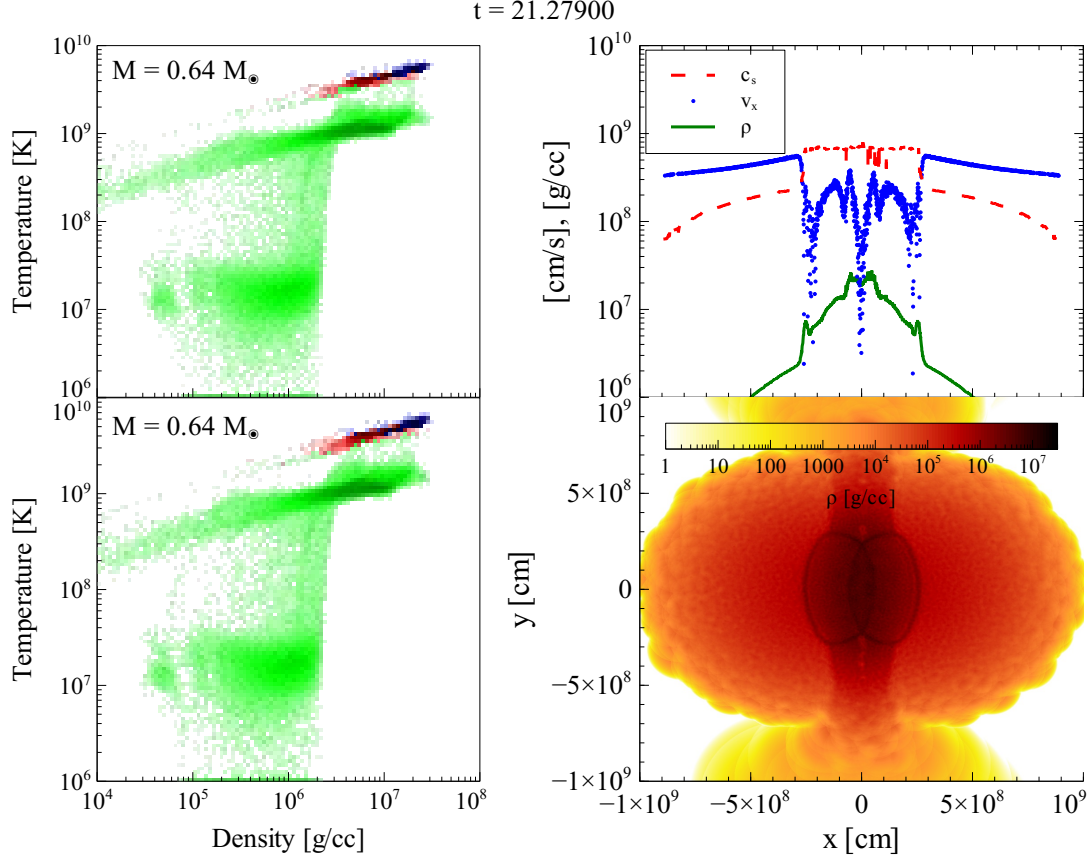
Figure 3.7: Same format as Figure 3.5, at a later time in the simulation.

The velocity structure preserves the isotopic segregation expected behind the burning front, with a progression from complete burning of carbon & oxygen to iron-peak elements, though silicon-group elements, and finally ending with an unburned or only partially burned carbon & oxygen envelope. This layered structure is in agreement with the observations of Scalzo et al. (2010) and others of type Ia SNe suspected of having been produced from double-degenerate progenitor scenarios.

The $b = 2$ scenario for this mass pair did not feature a detonation, and instead, resulted in a hot remnant embedded in a disk. Details of this simulation and its outcome will be discussed in §4.

Variations on Parameters

In order to assess the impact of the time-step on the nuclear yields, we compared three simulations of the $0.64\,M_\odot \times 2$, $b = 0$ case varying the value of f_u in Equation (3.1); one with a value
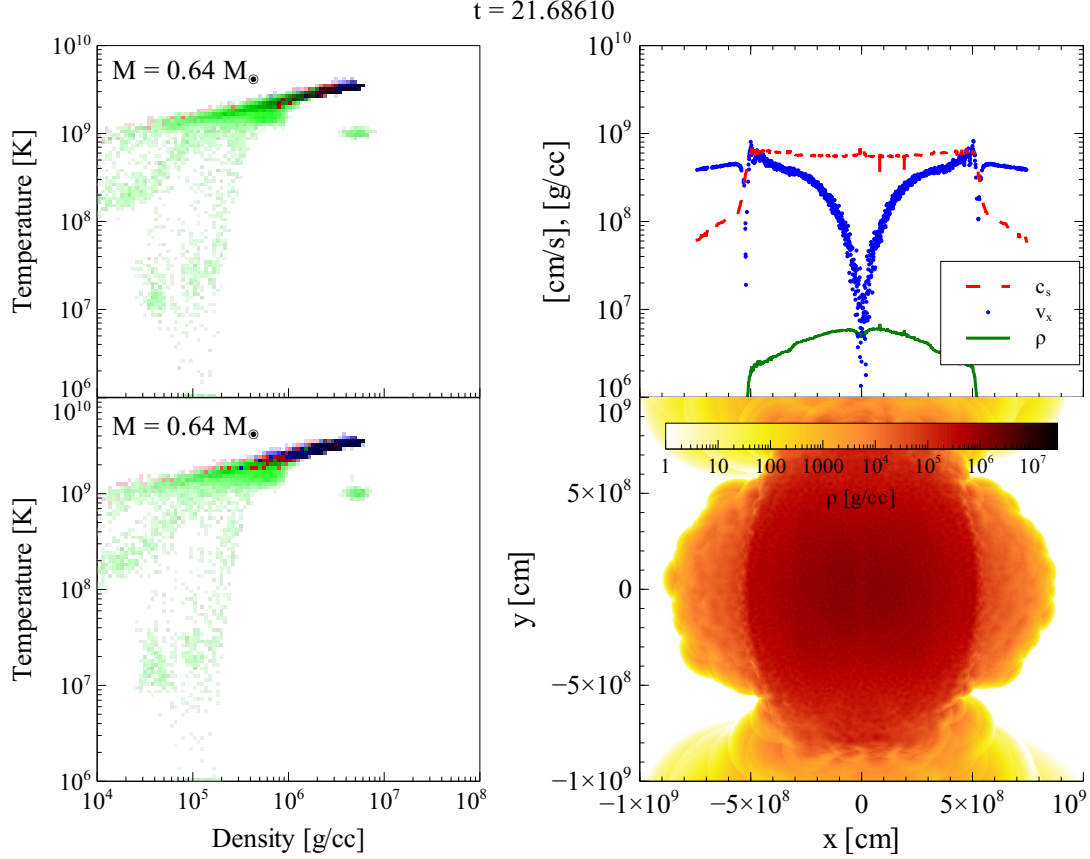
Figure 3.8: Same format as Figure 3.5, at a later time in the simulation.

of $f_u = 0.50$, another with $f_u = 0.30$, and finally, one with $f_u = 0.25$. As the results in table 3.3 show for the largest yields by mass, changes in the value of f_u below 0.5 have little discernible impact on the final outcomes.

Table 3.3: ^{56}Ni yields for $0.64\,M_\odot \times 2$, $b = 0$ simulations with variations on the parameter f_u and particle count.

f_u	Particle Count	^{56}Ni
0.50	2×10^5	0.51
0.30	2×10^5	0.51
0.25	2×10^5	0.51
0.30	1×10^4	0.21
0.30	4×10^4	0.31
0.30	4×10^5	0.49
0.30	2×10^6	0.53

The detonations on either side of the shocked region are unique to the $0.64\,M_\odot \times 2$ mass pairing and the $0.50\,M_\odot \times 2$ mass pairing described in §3.7. This is due, in large part, to the kinetic energy at impact, which is related directly to the infall speed. With greater infall speeds,
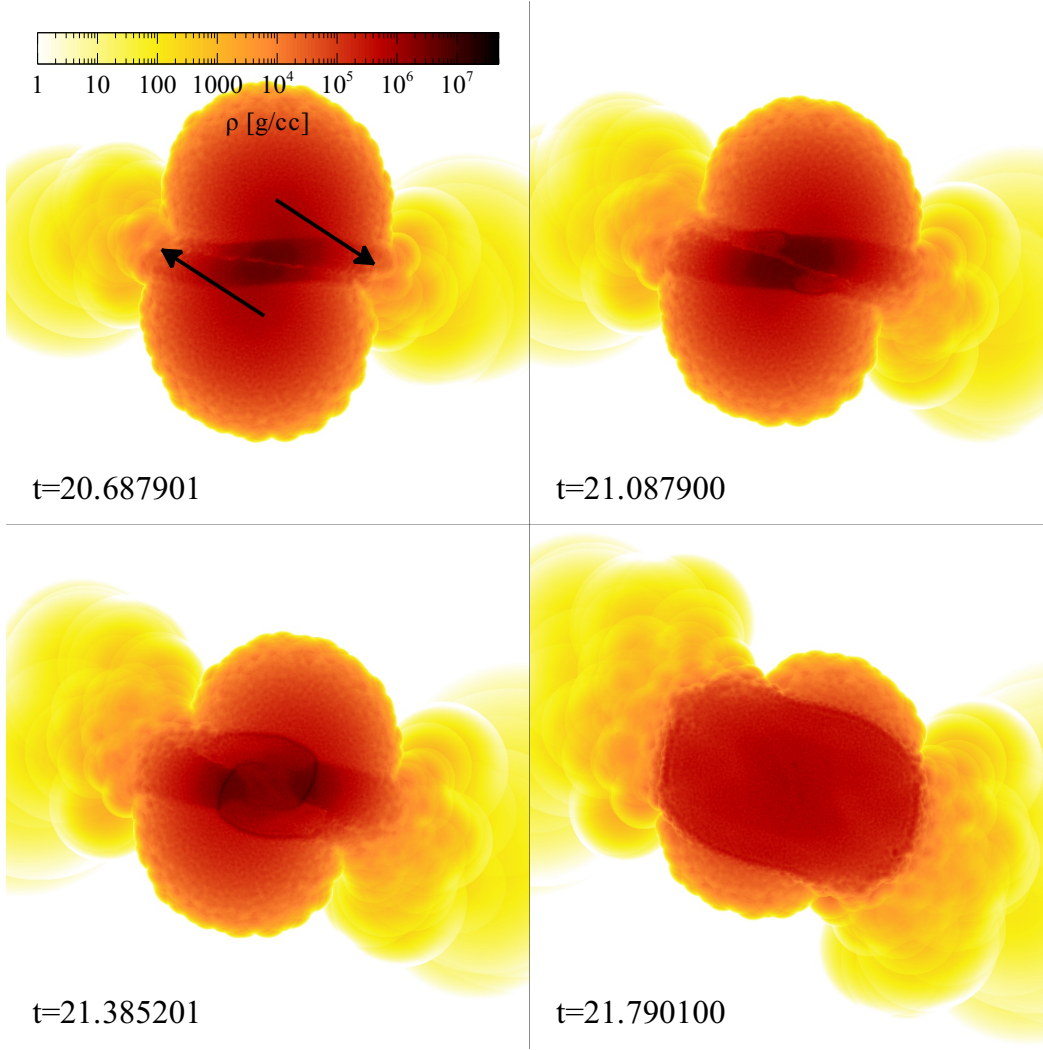
Figure 3.9: A 2D slice of interpolated densities through the x-y plane of the $b = 1$ case of two $0.64 \, M_\odot$ white dwarfs colliding. Four snapshots at different times are shown. Arrows in the top-left panel indicate the directions of motion of each star.

the shocked region heats sufficiently to initiate a detonation earlier, and the detonations begin nearer to the central region (the y-z plane).

We tested this mechanism with a $0.64 \, M_\odot \times 2$ collision scenario by giving the constituent stars an artificially high infall velocity to reproduce the kinematic energies associated with collisions of larger masses. In that test, the critical temperatures for carbon ignition were reached in locations nearer to the y-z plane, but still displaced enough that the pressure gradient was favorable to a detonation. In this case, the ^{56}Ni production was actually depressed, resulting in only $0.39 \, M_\odot$, due to an early detonation coupled with altered shock conditions.
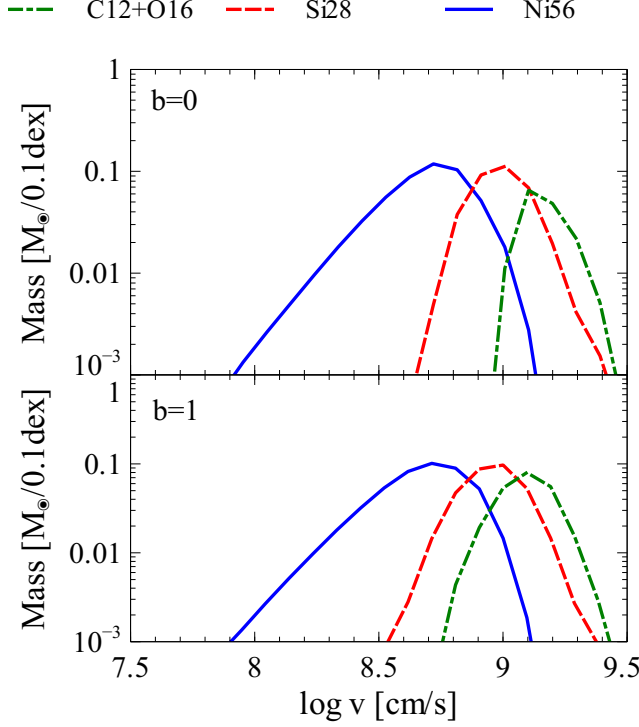
Figure 3.10: Masses of several isotopes at logarithmically spaced velocity bins for the $b = 0$ and $b = 1$ cases of mass pairing 1, $0.64\,M_\odot \times 2$.

We also tested the effect of velocity gradients (tidal distortions) on the final ^{56}Ni yield by running a $0.64\,M_\odot \times 2$, $b = 0$ collision with an initial separation of only $0.048\mathrm{R}_\odot$ with the commensurate relative velocities. In that simulation, the ^{56}Ni yield was also depressed, slightly, to $0.48\,M_\odot$. The combination of infall velocity and tidal distortions are evidently critical for ^{56}Ni production.

However, by far the most important parameter effecting the convergence of the ^{56}Ni yield is resolution. We carried out a convergence test of the ^{56}Ni yield in mass pair 1, $b = 0$, using equal-mass particle setups. We varied particle counts from 10^4 particles total, to 2×10^6. As Figure 3.11 demonstrates, convergence was reached at 2×10^5 particles. This compares favorably to previous convergence estimates in Raskin et al. (2009) that concluded $\sim 10^6$ particles were needed for convergence using equal-h particle setups.

Early work on numerical simulations of white dwarf collisions carried out by Benz et al. (1989b) did not have the benefit of modern computational resources to reach these kinds of resolutions. Consequently, the ^{56}Ni yields in those simulations were comparatively quite low.
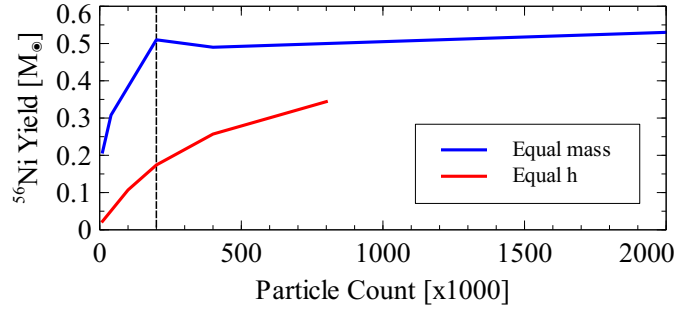
Figure 3.11: Convergence of the ^{56}Ni yield with particle count for simulations employing equal mass particles (blue, $0.64\,M_\odot \times 2$) and equal h particles (red, $0.6\,M_\odot \times 2$ from Raskin et al. 2009). The dashed, vertical line indicates the number of particles used in simulations throughout this paper.

Mass Pair 2 - $0.64\,M_\odot + 0.81\,M_\odot$

For asymmetrical collisions involving $0.64\,M_\odot$ and $0.81\,M_\odot$ white dwarfs, the higher kinetic energy with which they collide results in several, almost immediate detonations near the center in the $b = 0$ scenario. As Figure 3.12 shows, these detonation shocks superimpose to form a single, nearly spherical shock front that raises the sound speed above the infall speed for material in the $0.64\,M_\odot$ star, but the pressure gradient leftward of the detonation (region 1) stalls the detonation shock, which can be seen as a higher-density, laminar shock at the rightmost edge of region 1 in Figure 3.12.

However, region 1 does not maintain its lenticular shape as the two stars are moving at different speeds relative to this shocked region. This allows the detonation shock to travel through this region at $\approx$ Mach 1, eventually reaching fresh carbon outside of region 1. This fresh carbon ignites explosively, creating a second detonation (region 3 in Figure 3.13), which sends leading shocks back through region 1 and into region 2, shocking it a second time and eventually catching up with the first detonation shock.

Most of the ^{56}Ni in this scenario is produced in the more massive star, as Table 3.4 demonstrates. Since only low-density portions of the $0.64\,M_\odot$ star had entered the shocked region before the detonation, most of its contribution to the total output is in Si-group elements.

In the $b = 1$ case, the pre-detonation, shocked region reaches much higher densities, and the oblique angle at which the white dwarf stars enter the shocked region allows more material to become strongly shocked by the detonation. The detonation shock also twists
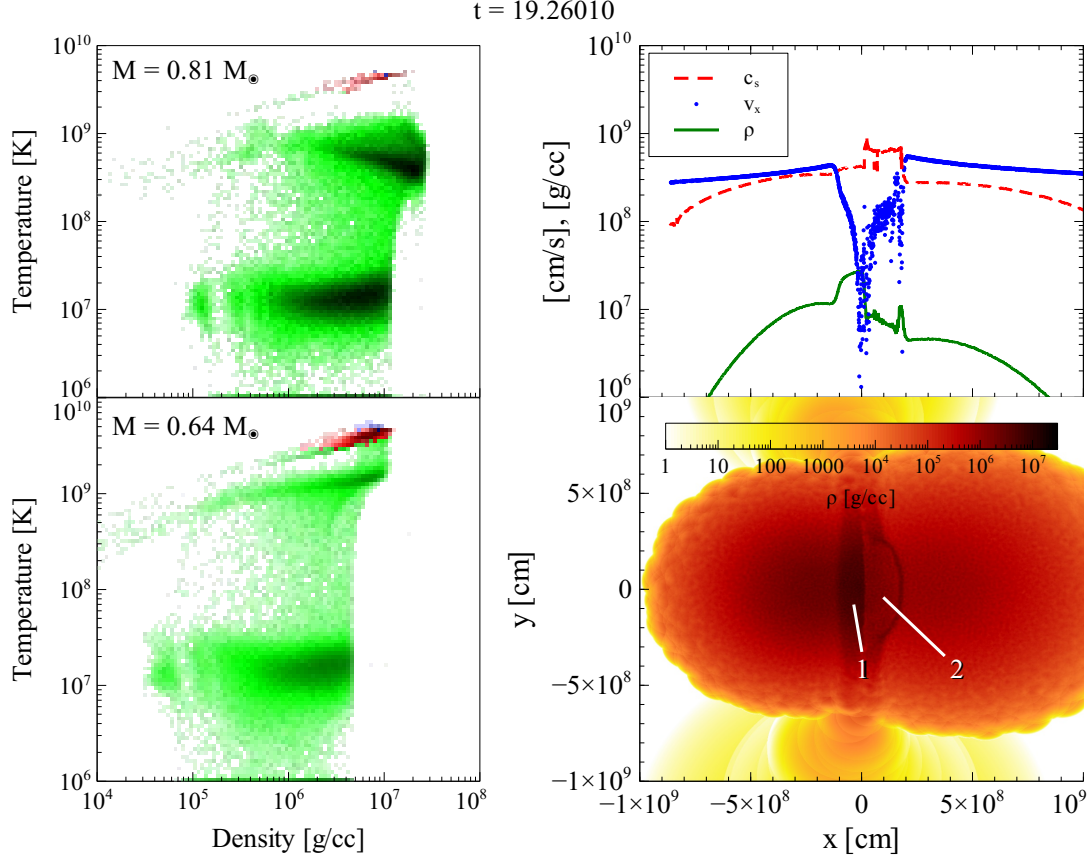
Figure 3.12: Same format as Figure 3.5 for mass pair 2, $0.64\,M_\odot + 0.81\,M_\odot$, and $b = 0$. Material shocked by the collision is labeled as region 1. Material behind the first detonation shock is labeled as region 2.

Table 3.4: Isotope yields for the $b = 0$ and $b = 1$ cases of mass pairing 2, $0.64\,M_\odot + 0.81\,M_\odot$.

b	Isotope	$0.81\ [M_\odot]$	$0.64\ [M_\odot]$	Total $[M_\odot]$
	^{12}C	0.21	0.03	0.24
	^{16}O	0.25	0.14	0.39
0	^{28}Si	0.12	0.27	0.39
	^{56}Ni	0.13	0.02	0.14
	^{12}C	0.02	0.03	0.05
	^{16}O	0.07	0.14	0.21
1	^{28}Si	0.12	0.25	0.37
	^{56}Ni	0.49	0.04	0.53

around the peculiar density contours inside the shocked region, shocking much of the material several times, as is seen in the bottom-right panel of Figure 3.14. The $0.81\,M_\odot$ star experiences a near complete burn of all of its carbon and oxygen. However, as in the $b = 0$ case, most of the $0.64\,M_\odot$ star remains unshocked at the time of the detonation breakout. As before, the $0.64\,M_\odot$ star contributes mostly Si-group elements to the total output, as shown in Table 3.4.
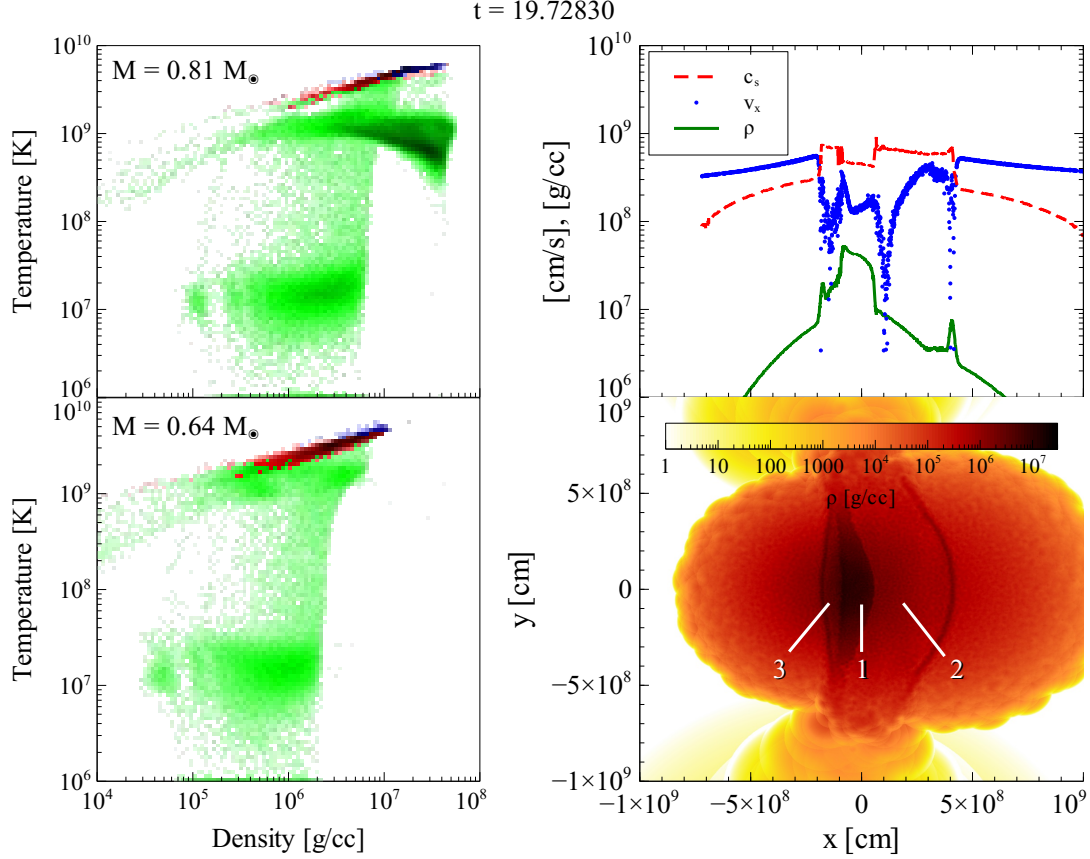
Figure 3.13: Same format as Figure 3.5 for mass pair 2, $0.64\,M_\odot + 0.81\,M_\odot$, and $b = 0$, at a later time in the simulation. Material shocked by the collision is labeled as region 1. Material behind the first detonation shock is labeled as region 2, and material behind the second detonation shock is labeled region 3.

The velocity profiles for the $b = 0$ and $b = 1$ cases of mass pair 2, shown in Figure 3.15, reinforce the observation that ^{56}Ni is created in a confined region in the $b = 0$ case, mainly in the densest portions of the shocked material from the $0.81\,M_\odot$ star. Carbon and oxygen, together, dominate the total output by mass, while in the $b = 1$ case, ^{56}Ni is the dominant isotope, followed by ^{28}Si.

Mass Pair 3 - $0.64\,M_\odot + 1.06\,M_\odot$

As with mass pair 2, the $b = 0$ case of mass pair 3 experiences a detonation of material in the $0.64\,M_\odot$ star very quickly after the stars first collide. However, owing to the greater potential well into which the $0.64\,M_\odot$ star is falling, the sound speed of the material shocked by the detonation is less than the infall velocity as shown in the top-left panel of Figure 3.16.
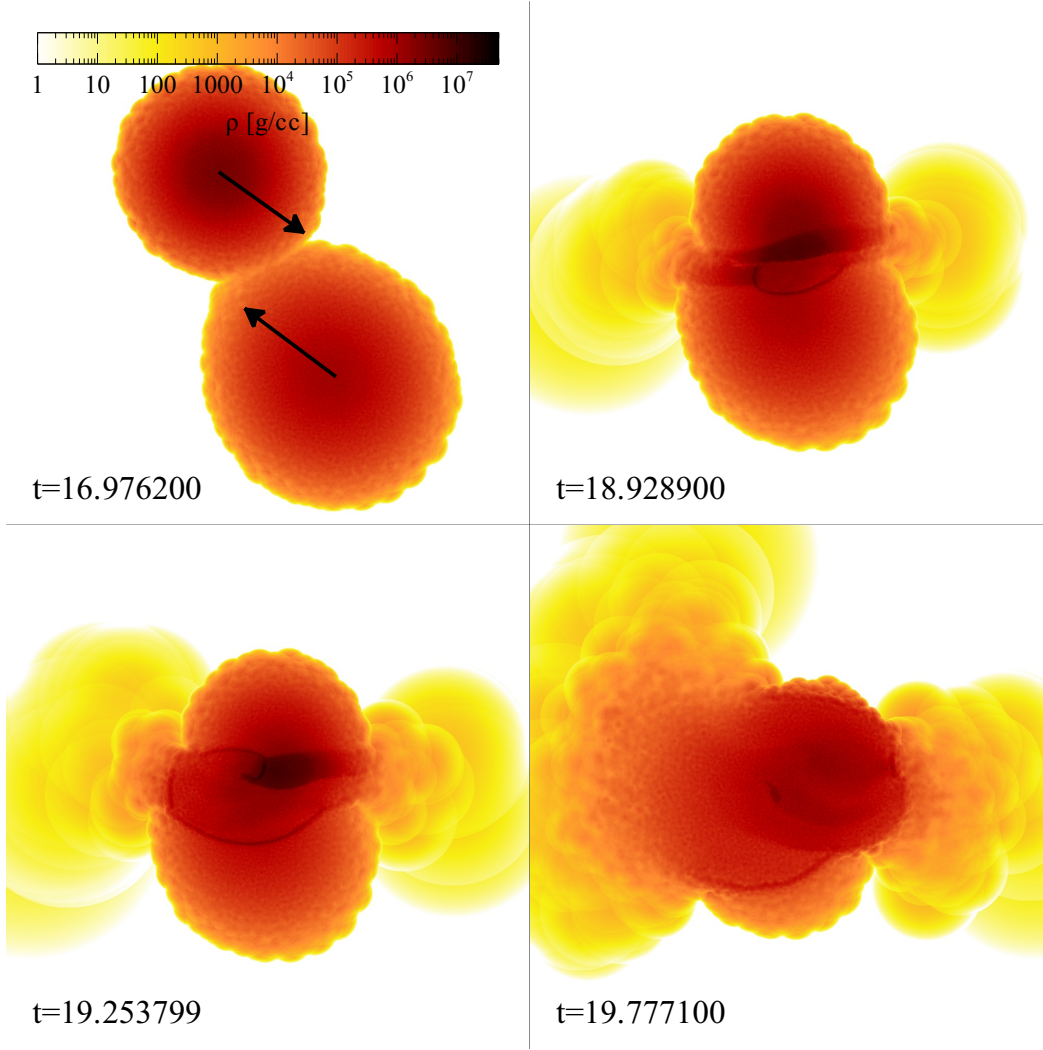
Figure 3.14: A 2D slice of interpolated densities through the x-y plane of the $b = 1$ case of a $0.64\,M_\odot$ white dwarf colliding with a $0.81\,M_\odot$ white dwarf. Four snapshots at different times are shown. Arrows in the top-left panel indicate the directions of motion of each star.

After ≈ 0.7s, as the core of the $1.06\,M_\odot$ star enters the shocked region, a second detonation lights on the left edge of the shocked region. This powers a shock that travels through both stars, catching up with the shock from the first detonation in the $0.64\,M_\odot$ star. The material in the $0.64\,M_\odot$ star burns mostly to ^{28}Si, while what burns in the $1.06\,M_\odot$ star burns almost entirely to ^{56}Ni, due to its higher density. The contributions from each star to the total elemental abundances are given in Table 3.5.

In simulations of mass pair 3 that introduced a non-zero impact parameter, the $1.06\,M_\odot$ star was simply too compact to be significantly disrupted by a collision with a $0.64\,M_\odot$ star. In both

Figure 3.15: Masses of several isotopes at logarithmically spaced velocity bins for the $b = 0$ and $b = 1$ cases of mass pairing 2, $0.64\,M_\odot + 0.81\,M_\odot$.

Table 3.5: Isotope yields for the $b = 0$ case of mass pairing 3, $0.64\,M_\odot + 1.06\,M_\odot$.

Isotope	1.06 $[\,M_\odot\,]$	0.64 $[\,M_\odot\,]$	Total $[\,M_\odot\,]$
^{12}C	0.39	0.02	0.41
^{16}O	0.40	0.15	0.55
^{28}Si	0.05	0.24	0.29
^{56}Ni	0.19	0.07	0.26

the $b = 1$ and $b = 2$ cases, most of the $1.06\,M_\odot$ star survived the collision, while completely disrupting the $0.64\,M_\odot$ star. Details of those simulations are given in §4.

Mass Pair 4 - $0.81\,M_\odot \times 2$

The symmetrical mass pair, $0.81\,M_\odot \times 2$ is quite unlike the $0.64\,M_\odot \times 2$ mass pairing discussed above. For the $0.81\,M_\odot \times 2$ mass pair with $b = 0$, several detonations occur in the y-z plane simultaneously and almost immediately after impact, owing to the higher temperatures reached in the shocked region from the higher infall speeds. As Figure 3.17 shows, these detonations superimpose and produce copious amounts of ^{56}Ni as they travel through the much denser material present inside the $0.81\,M_\odot$ stars. This denser material allows for a significantly greater
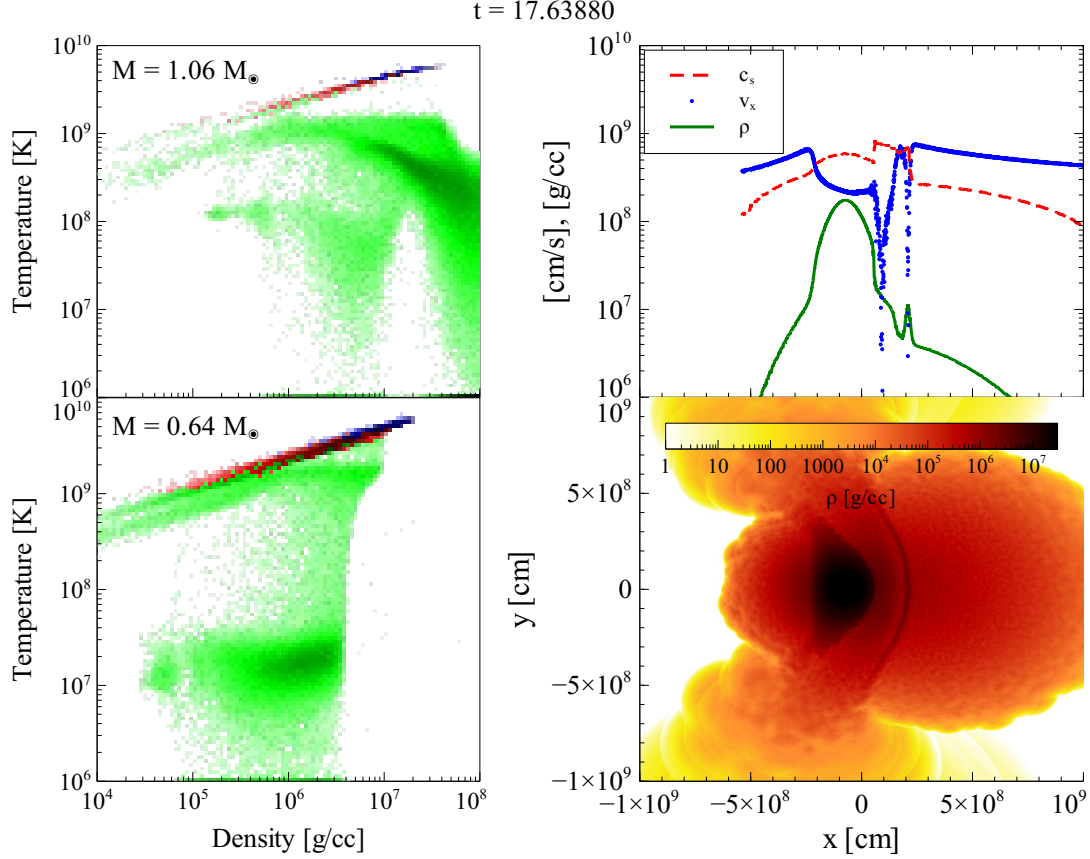
Figure 3.16: Same format as Figure 3.5 for mass pair 3, $0.64\,M_\odot + 1.06\,M_\odot$, and $b = 0$.

conversion of carbon and oxygen to ^{56}Ni. Therefore, with only a 26% increase in total mass of the system over the $0.64\,M_\odot \times 2$ scenario, there is a 64% increase in ^{56}Ni production to $0.84\,M_\odot$.

Having denser and more compact stars also reduces the sensitivity of the ^{56}Ni yield to impact parameter. Indeed, with two $0.81\,M_\odot$ stars, both the $b = 1$ and $b = 2$ simulations resulted in detonations and significant ^{56}Ni production, $0.84\,M_\odot$ and $0.65\,M_\odot$, respectively. Differences in the ^{56}Ni yield for the two non-zero impact parameter simulations stem mainly from the amount of material that burns to ^{28}Si before the detonations occur, with the $b = 2$ scenario featuring much more material burning at lower temperatures to silicon before the detonation. The high activation energy of ^{28}Si prevents much of that material from being converted to ^{56}Ni.

<center>Mass Pair 5 - $0.81\,M_\odot + 1.06\,M_\odot$</center>

The $0.81\,M_\odot + 1.06\,M_\odot$ mass pair follows a very similar pattern to that of mass pair 2 ($0.64\,M_\odot + 0.81\,M_\odot$). Intermediate impact parameters allow more material to enter the shocked region

t = 17.56160
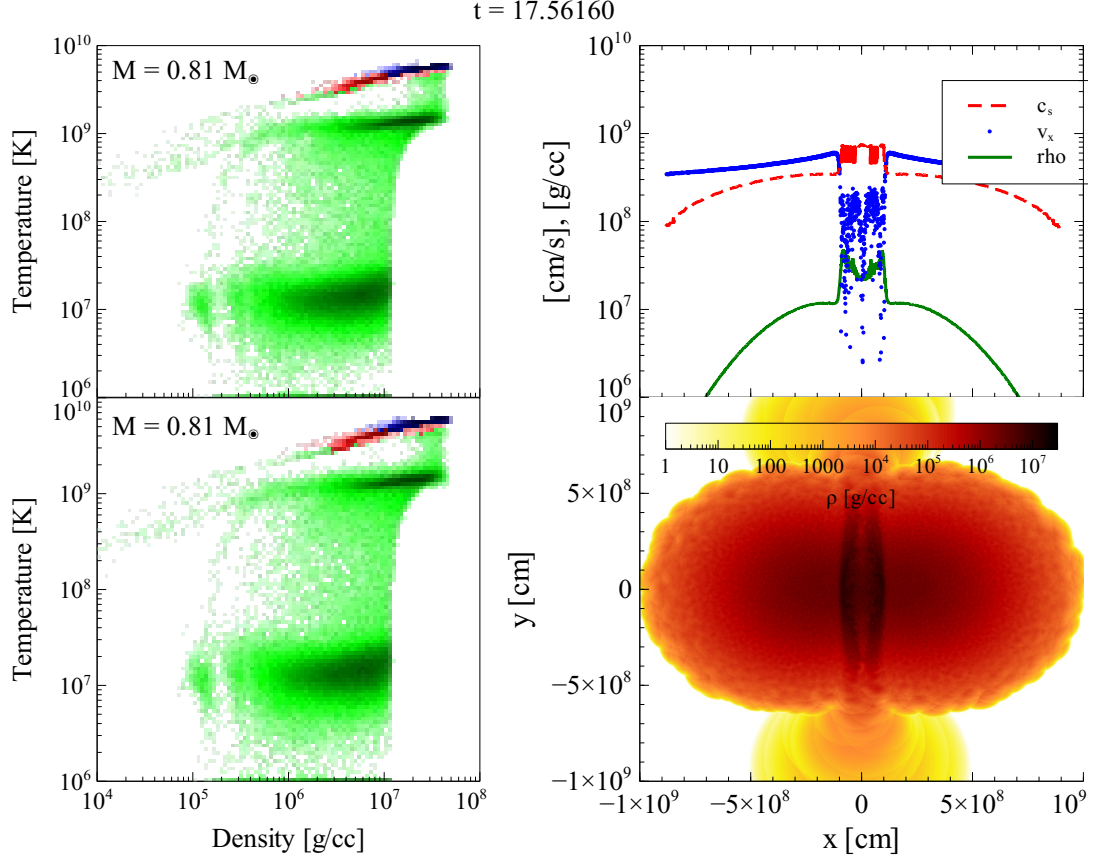
Figure 3.17: Same format as Figure 3.5 for mass pair 4, $0.81 \, M_\odot \times 2$, and $b = 0$.

before detonation, and so there is a rise in ^{56}Ni production in the $b = 1$ case over $b = 0$. However, because both stars involved in the collision are denser than their counterparts in mass pair 2, much more ^{56}Ni is produced overall. Contributions to the total yield in the $b = 0$ and $b = 1$ simulations are given in Table 3.6 below.

Table 3.6: Isotope yields for the $b = 0$ and $b = 1$ cases of mass pairing 5, $0.81 \, M_\odot + 1.06 \, M_\odot$.

b	Isotope	1.06 $[M_\odot]$	0.81 $[M_\odot]$	Total $[M_\odot]$
0	^{12}C	0.17	0.01	0.18
	^{16}O	0.19	0.09	0.28
	^{28}Si	0.06	0.22	0.28
	^{56}Ni	0.58	0.32	0.90
1	^{12}C	0.05	0.02	0.07
	^{16}O	0.07	0.09	0.16
	^{28}Si	0.06	0.22	0.28
	^{56}Ni	0.82	0.31	1.13

Mass Pairs 6 & 7 - $0.96\,M_\odot \times 2$ & $1.06\,M_\odot \times 2$

The $0.96\,M_\odot \times 2$ and $1.06\,M_\odot \times 2$ simulations were essentially similar to the $0.81\,M_\odot \times 2$ simulations with the exception that the greater the mass of the constituent stars, the less sensitive the ^{56}Ni yield was to impact parameter. Indeed, both mass pairs 6 and 7 produced almost the same yield in all three tested collision scenarios.

What distinguishes the $1.06\,M_\odot \times 2$ mass pair from all the others attempted is that the ^{56}Ni yield is super-Chandrasekhar in all cases. Were such explosions observed, there would be no doubt that a double-degenerate progenitor scenario of some kind was responsible. The resulting $1.71\,M_\odot$ of ^{56}Ni from the $1.06\,M_\odot \times 2$ simulations appear strikingly similar to the $1.7\,M_\odot$ of ^{56}Ni derived from the observations of Scalzo et al. (2010).

Mass Pair 8 - $0.50\,M_\odot \times 2$

Finally, we studied symmetric collisions of low-mass, $0.50\,M_\odot$ white dwarfs. Table 3.2 demonstrates that the $b = 0$ collision scenario for this mass pairing produced less than $0.01\,M_\odot$ of ^{56}Ni despite having resulted in a detonation. In this case, the energy generated from even mild carbon-burning was sufficient to unbind the stars. As in the $0.64\,M_\odot \times 2$, $b = 0$ scenario, the lower velocities with which the stars collide results in a late detonation. The shocked region slowly heats up until carbon-burning at its edges ignites a detonation.

It is clear from the velocity profile of the most abundant isotopes from this collision, given in Figure 3.18, that carbon and oxygen remain mostly unburned in this scenario. This seems to suggest that collisions of low-mass white dwarfs ($M \lesssim 0.6\,M_\odot$) of the CO variety would not produce observable transients. Other simulations introducing impact parameters with this mass pair were not attempted with carbon-oxygen white dwarfs as the $b = 0$ simulation yielded essentially a non-result. However, further investigation involving Helium white dwarfs is warranted.

3.4   Results & Analysis II - Remnants

As seen in Raskin et al. (2009), the $b = 2$ case of mass pair 1 ($0.64\,M_\odot \times 2$) did not feature a detonation and instead formed a hot remnant of thermally-supported carbon and oxygen with some carbon-burning products. Figure 3.19 illustrates the dynamics of this collision, starting
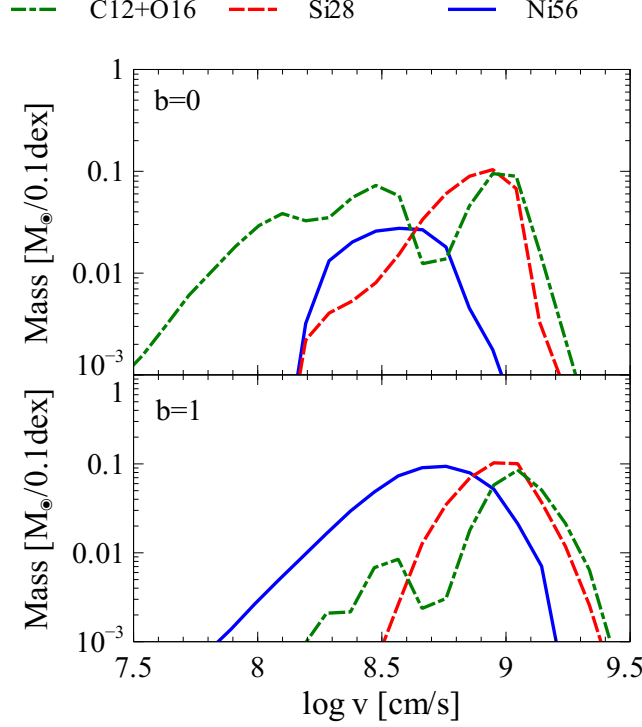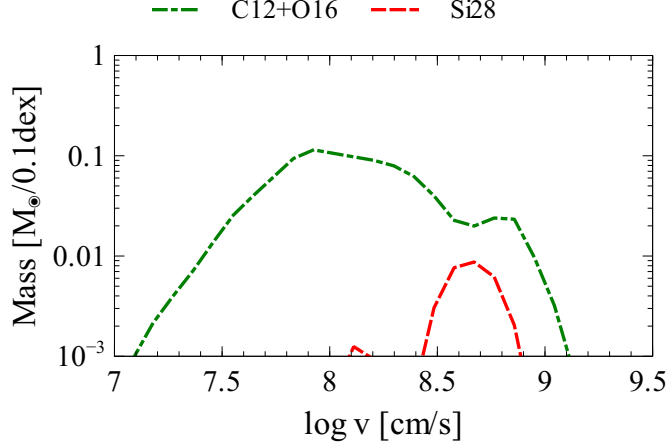
Figure 3.18: Masses of several isotopes at logarithmically spaced velocity bins for the $b = 0$ case of mass pairing 8, $0.50\,M_\odot \times 2$.

with a glancing case that leads to the constituent stars spinning off from each other before coalescing into a single hot object.

The compact remnant core after 100s featured a nearly constant density of $\rho \sim 10^6$ g cm^{-3}. It was surrounded by a thick, Keplerian disk $\approx 2.0 \times 10^{10}$ cm in radius with a scale radius $r_0 \approx 2.3 \times 10^9$ cm. The compact object at the center of the disk is not strictly a white dwarf since much of its pressure support is thermal ($T \approx 5 \times 10^8$ K). Indeed, since degeneracy pressure support necessitates that more massive white dwarfs are smaller than less massive ones, this object, at $\approx 0.8\,M_\odot$ is far too large to be wholly degenerate ($r_{rem} \approx 2.5 \times 10^9$ cm); larger than the $0.64\,M_\odot$ white dwarfs that entered into the collision ($r_{0.64} = 6.98 \times 10^8$ cm).

Carbon ignition nominally takes place at approximately 7-8$\times 10^8$ K (e.g. Gasques et al. 2007), but recent phenomenological models (e.g. Jiang et al. 2007) have suggested a strongly reduced, low-energy astrophysical S-factors for carbon fusion reactions that potentially reduce carbon ignition temperatures to $\approx 3 \times 10^8$ K, especially at densities of 10^9 g cm^{-3}. A lower carbon burning threshold would be of interest to future studies of collision remnants.

Since the system started in a bound state, ($T \lesssim -V$, where T in this case is total kinetic energy and V is total gravitational potential energy) and since any energy gained from nuclear processes is negligible, most of the material cannot escape the system and the disk remains bound to the compact core. It will eventually cool and collapse onto the surface of the compact object. However, the hot core may accelerate parts of the disk to escape velocity via radiative
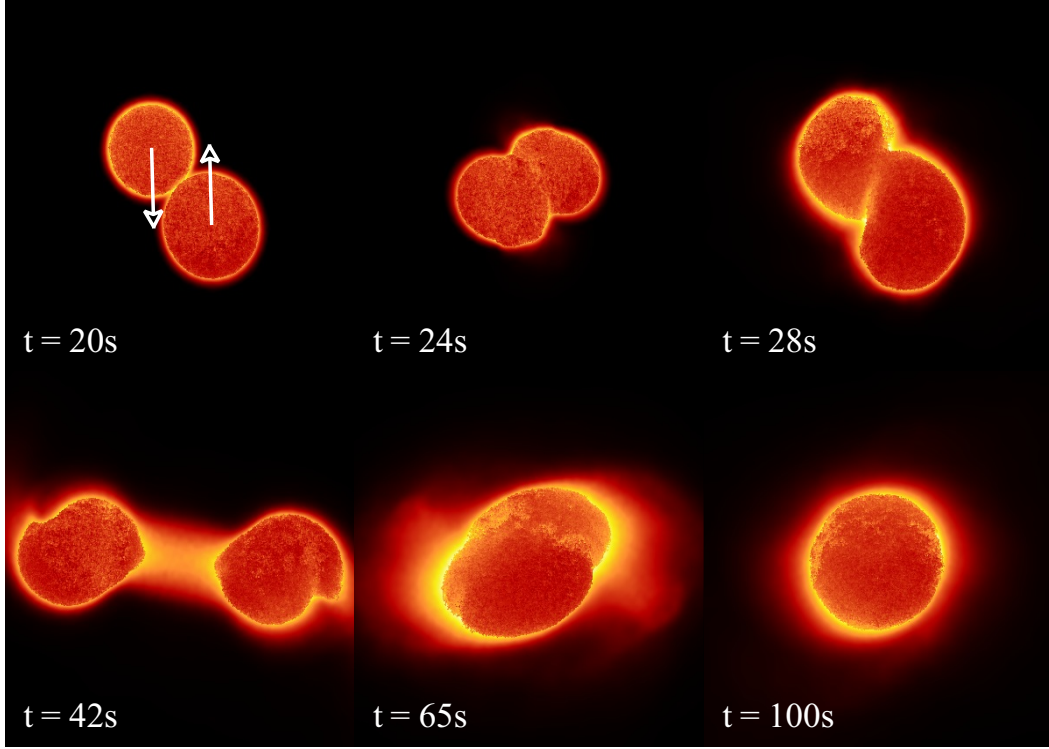
Figure 3.19: Snapshots of density isosurfaces at six different times for the $b = 2$ simulation of mass pair 1, $0.64\,M_\odot \times 2$. After first colliding, the stars separate before coalescing into a single object.

processes, and so the calculation of the final mass of the resultant white dwarf is beyond the scope of this paper. Suffice it to say, the final mass will not exceed the Chandrasekhar limit as only $1.28\,M_\odot$ of material is available.

For the $b = 2$ case of mass pair 2, $0.64\,M_\odot + 0.81\,M_\odot$, the compact remnant was slightly less massive at $\approx 0.75\,M_\odot$. However, since the total mass of the system is super-Chandrasekhar, the final remnant mass may result in a super-Chandrasekhar white dwarf. Again, this final mass will depend greatly on radiative processes, and the likelihood of producing a SNIa will hinge on the accretion rate of the disk onto the core.

The simulations of mass pair 3, $0.64\,M_\odot + 1.06\,M_\odot$, resulted in remnants in both the $b = 1$ and $b = 2$ cases as the $1.06\,M_\odot$ white dwarf was too compact for the star to be much affected by a grazing collision with a $0.64\,M_\odot$ white dwarf. In the $b = 1$ case, some of the atmosphere of the $1.06\,M_\odot$ star was stripped away to join the material from the disrupted $0.64\,M_\odot$ star in the disk, while in the $b = 2$ case, the $1.06\,M_\odot$ star was nearly unaffected by the collision. Figure 3.20 illustrates that the remnant core of the $b = 2$ simulation masses $\approx 1.0\,M_\odot$,

and the central densities are essentially unchanged from the $1.06\,M_\odot$ progenitor.
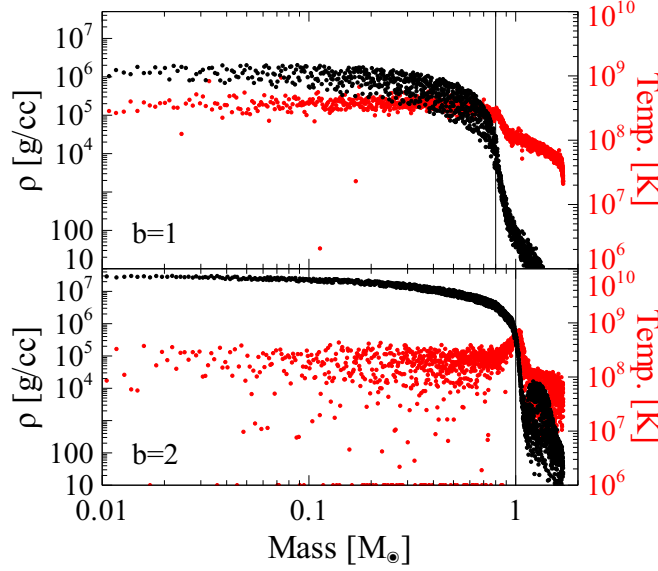
Figure 3.20: Temperature and density profiles of the $b = 1$ and $b = 2$ simulation remnants of mass pair 3, $0.64\,M_\odot + 1.06\,M_\odot$.

Some features worth noting in the $b = 2$ profiles in Figure 3.20 are the indications of a cold core ($T_{core} \approx 2 \times 10^8$ K) surrounded by a hot envelope ($T_{env.} \approx 9 \times 10^8$ K), and the presence of a strong overdensity in a part of the disk, which causes large spreads in density and temperature for the disk material. This suggests that while the $0.64\,M_\odot$ star is no longer a gravitationally bound object, it has nevertheless not been completely disrupted.

The radial profiles of the $b = 2$ simulation of the $0.81\,M_\odot + 1.06\,M_\odot$ mass pair, shown in Figure 3.21, indicate a very similar structure, with a high-temperature envelope surrounding a cold core and an overdensity in a part of the disk. These inhomogeneities in the disk would most likely vanish after many crossing-times, however, it is highly unlikely that radiative processes or collisional excitations within the disk could remove as much as $0.4\,M_\odot$. This suggests that after a Kelvin-Helmholtz timescale, the remnant from the $b = 2$ collision of mass pair 5 will almost certainly be super-Chandrasekhar.

Some of the properties of these remnants are very similar to the simulated remnant explored in Yoon et al. (2007), which was produced by the merger of $0.9\,M_\odot$ and $0.6\,M_\odot$ white dwarfs. In that simulation, the remnant also featured a cold core ($T_{core} \approx 1 \times 10^8$ K) surrounded by a hot envelope ($T_{env.} \approx 6 \times 10^8$ K), embedded inside a thick, Keplerian disk. Using a 1D stellar evolution code, they found that such systems can indeed evolve on timescales $\sim 10^5$yr
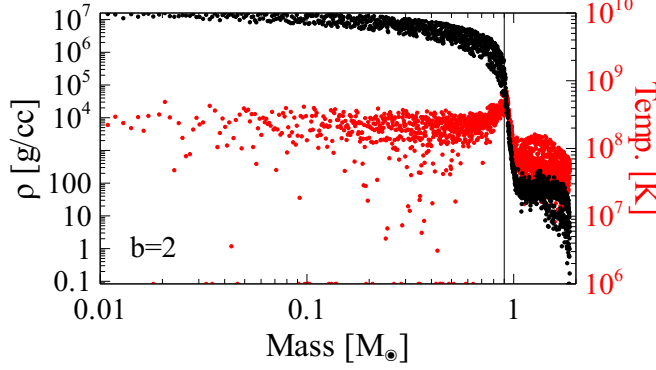
Figure 3.21: Temperature and density profiles of the $b = 2$ simulation remnant of mass pair 5, $0.81\,M_\odot + 1.06\,M_\odot$.

toward becoming SNeIa.

3.5   Discussion

White dwarf collisions are not typically regarded as SNeIa progenitors, and therefore, they have been relatively unexplored theoretically. Here we have conducted a comprehensive suite of simulations of such collisions examining the dependence of their ^{56}Ni yield on total mass, mass ratio, and impact parameter. Our results suggest that white dwarf collisions are a viable avenue for producing SNeIa with brightnesses that range from sub-luminous to super-luminous.

In fact, in more than 75% of our simulations, collisions resulted in detonations, and in all but the least massive combination of stars, significant amounts of ^{56}Ni were produced. We found that even mass pairs that are below the Chandraskehar limit featured explosive nuclear burning, with the $0.64\,M_\odot \times 2$ mass pair producing ^{56}Ni in quantities comparable to standard SNeIa. Moreover, the most massive combinations of stars produced super-luminous quantities of ^{56}Ni, regardless of the impact parameter, greatly increasing their likelihood of detection. The ^{56}Ni yields from these collisions are consistent with those of observed SNeIa with super-Chandrasekhar mass progenitors.

Asymmetric mass pairs generally produced less ^{56}Ni in head-on collisions than symmetric pairs. At middling impact parameters, much more ^{56}Ni was produced, however, at high impact parameters, there was little or none. This is due primarily to the delicate balance which must be struck between the dynamics of the impact and the binding energy of the less massive star in order to establish a stalled shock region that can lead to a detonation. At high impact

51

parameters, the less massive star is typically unbound by the collision before much or any ^{56}Ni is produced.

For combinations of masses and impact parameters that did not detonate, the end result always featured a compact, semi-degenerate object surrounded by a bound, thick disk of carbon and oxygen. Many of these systems were super-Chandrasekhar, and over Kelvin-Helmholtz time scales, these, too, are candidate progenitors for producing SNeIa. These remnant objects are very similar to those described as resulting from mergers of white dwarfs. We will return to the discussion of these types of remnants in the next chapter that explores mergers in detail.

Our results have shown that ^{56}Ni production in white dwarf collisions is a non-linear process that depends on several factors, including infall velocities and tidal distortion effects. Foremost among parameters to be explored in future studies is the composition of the constituent white dwarfs. Helium has a much lower activation energy than carbon or oxygen, and combinations of stars that include helium white dwarfs would almost certainly produce interesting and different results. Other avenues to be explored include the impact of more detailed modeling of the isotopic profiles in the progenitor stars, and the possibility of sparse hydrogen atmospheres. The results of these studies will shed further light on the contribution of double-degenerate collisions to the observed population of SNeIa.

Chapter 4

DOUBLE DEGENERATE WHITE DWARF MERGERS AND REMNANTS

In this chapter, we continue the series of numerical studies of progenitor mechanisms and present the results of simulation studies of white dwarf mergers as possible type Ia supernova progenitors. Using SNSPH, we carry out a comprehensive simulation survey of double-degenerate white dwarf binary mergers of varying mass combinations in order to establish correspondence between initial conditions and remnant configurations. We find that all of our simulation remnants share some general properties such as a cold, degenerate core surrounded by a hot disk, while some remnants exhibit cores that will grow to become super-Chandrasekhar masses after cooling and before viscosity-driven accretion. We show that the disks that result from our simulations are too hot to be treated with typical thin disk accretion rates. We also find that some of our simulations with very massive constituent stars exhibit helium detonations on the surface of the primary star before complete disruption of the secondary.

4.1 Introduction

Type Ia supernovae are commonly accepted to be the observed transient produced after a thermonuclear detonation inside a white dwarf star. While the preferred mechanism for producing SNeIa involves accretion from an evolved main sequence star onto a white dwarf (Whelan & Iben 1973; Nomoto 1982; Hillebrandt & Niemeyer 2000), the observed SNeIa rate is incompatible with the narrow range of helium accretion rates that will initiate a carbon detonation as opposed to accretion induced collapse or classical novae (Nomoto & Kondo 1991). Moreover, many recent observations of abnormally luminous SNeIa have been interpreted as having derived from double-degenerate systems involving two white dwarfs.

Photometric observations of SN 2007if suggest $1.6\pm0.1\,M_\odot$ of ^{56}Ni was formed, implying a progenitor mass of $2.4\pm0.2\,M_\odot$ (Scalzo et al. 2010), which is well above the Chandrasekhar limit (Chandrasekhar 1931). Spectroscopic observations of SN 2009dc suggest $\gtrsim 1.2\,M_\odot$ of ^{56}Ni (Tanaka et al. 2010), depending on the assumed dust absorption. Since $0.92\,M_\odot$ of ^{56}Ni is the greatest yield a Chandrasekhar mass can produce (Khokhlov et al. 1993), this yield also implies a super-Chandrasekhar progenitor mass. And observations of SN 2003fg by Howell et al. (2006) and of SN 2006gz by Hicken et al. (2007) infer $\sim 1.3\,M_\odot$ of ^{56}Ni each.

Generally, for the purposes of cosmological measurements, obvious double-degenerate

candidates are excluded from SNeIa surveys. The Phillips relation, which established SNeIa as standard candles (Phillips 1993), relates the peak luminosity of a SNIa to the change in magnitude after 15 days (or the stretch). This relation is often thought to be the result of a balance struck between the ^{56}Ni yield and the opacity of the ejecta material, assuming a total mass not exceeding the Chandrasekhar mass. However, since a double-degenerate system can have essentially any mass up to two times the Chandrasekhar mass, the relationship between the ^{56}Ni yield and the ejecta mass is not constant, and therefore, the Philips relation may not be applicable to these SNeIa. SNeIa deriving from double-degenerate progenitor systems can have ordinary ^{56}Ni yields, and thus may be masquerading as typical SNeIa, introducing systematic errors into cosmological surveys. In order for SNeIa to remain premiere distance indicators, we must first establish whether double-degenerate SNeIa are standardizable, and if not, we must identify the tell-tale signatures of a double-degenerate progenitor mechanism.

The most probable double-degenerate progenitor scenario involves two white dwarfs in a tight binary, though other progenitor systems have been considered (Benz et al. 1989a; Raskin et al. 2009; Rosswog et al. 2009). Binary white dwarf systems were first seriously explored as plausible SNeIa progenitors by Iben & Tutukov (1984) and Webbink (1984). In such a system, tidal dissipation and gravitational radiation drive the binary pair into an ever closer orbit. Eventually, the least massive white dwarf, being physically larger as $R \propto M^{-1/3}$, overflows its Roche lobe and begins to accrete material onto the primary, or more massive companion star. For many mass combinations, this is a fundamentally unstable process in which the loss of mass from the secondary causes it to outgrow its Roche lobe faster than its orbit widens due to conservation of angular momentum (see e.g. Marsh et al. 2004).

Benz et al. (1990) performed one of the first simulations of double-degenerate mergers, examining a binary system consisting of a $1.2\,M_\odot$ white dwarf primary and a $0.9\,M_\odot$ white dwarf secondary. They used a smooth particle hydrodynamics code with 3000 particles per star and found that the merger remnant consisted of a $1.7\,M_\odot$ core surrounded by a rotationally supported disk. This is more massive than the Chandrasekhar limit, but they concluded that the central object was not entirely degenerate, having been considerably heated, and thus, much of the object's support against gravitational collapse came simply from thermal pressure.

Since this pioneering work, others have revisited the white dwarf merger scenario with up-to-date simulation codes and higher resolutions than were possible in the past (see e.g. Yoon

et al. 2007; Lorén-Aguilar et al. 2009). In this chapter, we will also revisit white dwarf mergers, examining a wider range of possible mass combinations than previously studied, and using more realistic white dwarf compositions in each of our simulations. The structure of this chapter is as follows. In §2, we will review and compare our method to those used in previous studies of white dwarf mergers. We discuss the results of our simulations in §3, and finally, in §4, we summarize our results and conclusions.

4.2   Method & Initial Conditions

As in the previous chapter on white dwarf collisions, we employ the 3D smooth particle hydro-dynamics code SNSPH (Fryer et al. 2006). Particle codes are ideally suited to simulating binary systems as they excel at conserving angular momentum, which is crucial for properly simulating accretion flows in binary systems. We include a Helmholtz free energy equation of state (EOS; Timmes & Arnett 1999; Timmes & Swesty 2000) that spans a range of possible thermodynamic conditions, from cold, electron-degenerate gas, to hot, non-degenerate gas, and includes coulomb corrections and photon pressures. For nucleosynthesis, we use a 13-isotope, α-chain nuclear net-work with a hybrid photo-disintegration capture scheme as described in Raskin et al. (2010), which utilizes a similar method for sub-cycling the reaction rates to what is implemented in MAESTRO (Nonaka et al. 2010). We limit our hydrodynamic time step to that which results in at most a 30% change in internal energy (u) due to nuclear reactions. If nuclear reactions are not important, the time step is not allowed to grow larger than what is derived from the Courant-Friedrichs-Lewey condition.

For our constant mass particle arrangements, we use Weighted Voronoi Tessellations (WVT; Diehl & Statler 2006), which ensures the lowest energy particle configuration for our stars. We initiate each of our carbon-oxygen white dwarfs with a uniform composition of 50% ^{12}C and 50% ^{16}O plus a thin atmosphere of pure ^{4}He that comprises 10% of the total stellar mass. Each of our stars is relaxed to an isothermal temperature of roughly 10^7 K.

There is some debate over whether white dwarfs in tight binaries will be tidally locked. The time scales for inspiral and for spinning up the white dwarfs are roughly commensurate. Yoon et al. (2007) initialized their binary systems with tidally locked white dwarfs, while Lorén-Aguilar et al. (2009) assumed they would not be. Since most observations of close white dwarf binaries have suggested they are tidally locked, we make a conscious choice to simulate our binaries in a tidally locked configuration. We initially allow our stars to fall from rest toward

each other until there is noticeable tidal distortion in the least massive star. This is done via an iterative process whereby the stars free-fall for a short time, and then all particles have their velocities reset and free-fall begins again. This ensures that the binary system is in a meta-stable configuration and that the stars are still in hydrostatic equilibrium after tidal distortions have first appeared.

This method avoids unnaturally high accretion rates that result from the secondary white dwarf overflowing its Roche lobe immediately upon the start of the simulation. Figure 4.1 shows the effective potential at $t = 0$ in the rotating frame of the $0.64\,M_\odot + 0.81\,M_\odot$ merger simulation, where $\Phi_{eff} = \Phi_g - 1/2\Omega^2 r^2$ normalized to 1.79×10^{17} erg/g with Ω being the orbital velocity. As is evident, none of the particles in the $0.64\,M_\odot$ star lie outside of the Roche lobe, and no particle has a higher potential than the potential wall between the two stars. Dan et al. (2011) discuss how previous efforts in this area have overestimated the accretion rates due to inappropriate initial conditions, and this can have implications for the final arrangement of the system and on the long-term evolution prospects.

Our iterative method for creating the initial conditions of the mergers avoids immediate and rapid mass-transfer while also placing the stars very near the stage where mass transfer would naturally begin. At this stage, the stars are set into their tidally locked orbits about their common center of mass with the initial periods given in Table 4.1 for each of our chosen mass combinations. Over several orbits, the tidal distortions grow and material from the secondary star overflows its Roche lobe and mass transfer begins. Our mass combinations all lie safely in the regime of unstable mass transfer (Marsh et al. 2004), and so resolving a steady accretion stream that could possibly lead to stable accretion using a discretized method like SPH is not important.

Table 4.1: Simulated binary mass pairs and their initial orbital periods (τ_0). All masses are solar.

#	m_1	m_2	m_{tot}	m_1/m_2	τ_0 [s]
1	0.64	0.64	1.28	1.00	47.61
2	0.64	0.81	1.45	0.79	46.99
3	0.64	0.96	1.60	0.67	42.71
4	0.64	1.06	1.70	0.60	43.99
5	0.81	0.81	1.62	1.00	28.72
6	0.81	0.96	1.77	0.84	27.83
7	0.81	1.06	1.87	0.76	25.34
8	0.96	0.96	1.92	1.00	21.50
9	0.96	1.06	2.02	0.90	17.95
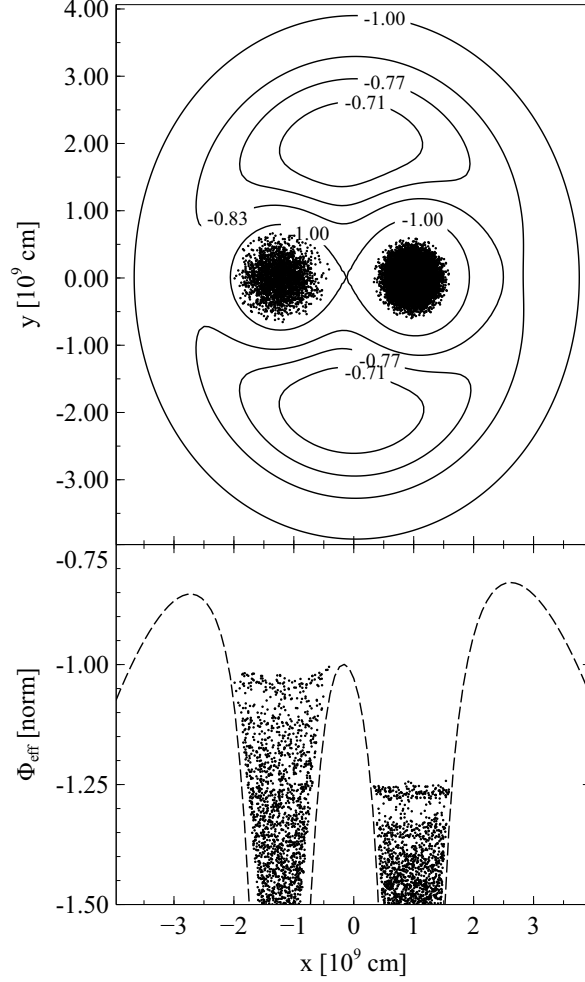
Figure 4.1: Top panel: Particle positions for a representative subsample of all particles overlaid on top of a contour map of the rotating frame effective potential in the initial conditions ($t = 0$) of the $0.64\,M_\odot + 0.81\,M_\odot$ merger simulation. The effective potential is normalized to -1 at the location of the Roche lobe contact between the two stars (L1). Bottom panel: Particle x-positions vs. effective potentials are plotted with the derived potential for the same conditions and normalization as the top panel. Inset: Same as bottom panel, but rescaled to better demonstrate the potential difference between the particles of the $0.64\,M_\odot$ star and the point of Roche lobe contact.

Pakmor et al. (2010) also explored a double degenerate merger of two $0.9\,M_\odot$ white dwarfs in a simulation study that was the first of its kind to track a merger from the initial inspiral to the final detonation and subsequent homologous expansion phase. They found that if such a meger features a prompt detonation before settling into a meta-stable core-disk configuration, the resultant supernova would be exceptionally dim, appearing much like 1991 bg. However, the detonation in their simulations was inserted by hand at the location where large-scale conditions

matched those found in offline calculations to produce microphysical conditions necessary for detonation.

At first glance, this is a reasonable approach since the length-scale required for sustaining a detonation is quite small and unresolved in an SPH simulation. While the conditions across a single particle may not be sufficient to initiate a detonation on their own, it is reasonable to suspect that unresolved temperature fluctuations could lead to a detonation that would not be captured in a simulation like this. However, it is not clear that these large-scale conditions always lead to a detonation and so should be detonated manually. In fact, as will be discussed, many of our simulations produced the same detonation preconditions in local hotspots at the surface of the accretor star, but these hotspots were not gravitationally constrained as they were part of an orbiting flow. Instead, they merely expanded outward hydrodynamically and floated away from the surface, cooling rapidly. For this reason, we choose not to insert detonations into those hotspots while leaving the question open as to whether prompt detonations in these scenarios are likely or unlikely.

4.3   Results & Analysis

In our simulations of equal-mass binaries, such as simulation 5 with $0.8\,M_\odot \times 2$, depicted in Figure 4.2, there is first a protracted accretion phase that persists for several orbits. During this time, both stars lose material, and thus angular momentum, through the L2 and L3 points. This brings the stars closer together, hastening their mass loss. The helium atmospheres that the stars were initially given also burns fairly rapidly to carbon and oxygen during this phase. Finally, one of the stars is disrupted entirely, owing primarily to slight inhomogeneities in the constituent stars. At this stage, $\approx 2\%$ of the carbon is burned into heavier, silicon-group elements. The iron-group yield from the merger is negligible.

After many orbital periods, the system settles into a meta-stable configuration with a dense core, a shock-heated, sub-keplerian disk, and a semi-degenerate interface between them. As Figure 4.3 indicates, much of the core has been heated slightly to $\approx 2 \times 10^8$ K, while the interface reaches temperatures near 10^9 K. The core and interface also exhibit solid-body rotation out to $\approx 1.05\,M_\odot$.

While the disk is large in spatial extent with an outer radius of $\approx 0.8 R_\odot$, it represents $\approx 35\%$ of the total system mass, or $\approx 0.57\,M_\odot$. Moreover, most of the mass of the disk lies
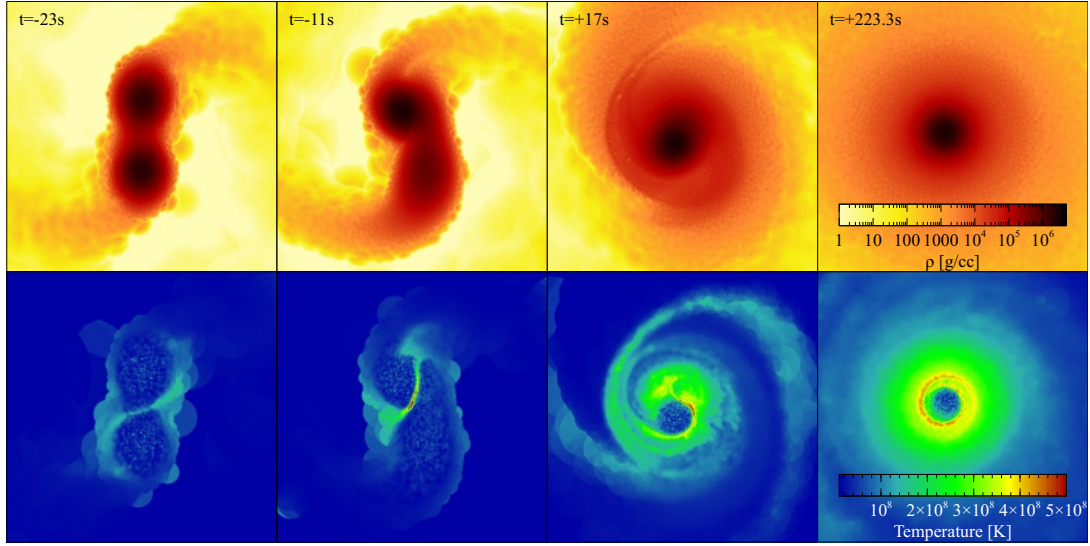
Figure 4.2: Snapshots in time of simulation 5, $0.8\,M_\odot \times 2$, with the time coordinate centered on the moment of complete destruction of the secondary star. The top four images are density maps of slices in the x-y plane, while the bottom four images are temperature maps of the same slice.

much nearer to the core, with the half-mass radius at $\approx 0.02 R_\odot$, as compared to the radius of the core, $\approx 0.008 R_\odot$. This disk will eventually decay due to viscosity and angular momentum transfer, and often an α-disk prescription for the viscosity is used to compute the time scale for this accretion (Shakura & Sunyaev 1973). The α-disk accretion time can be approximated by

$$\tau_{acc} \simeq \alpha^{-1} \left(\frac{r_d}{2h} \right)^2 \Omega^{-1}, \tag{4.1}$$

where α is a free parameter that relates the viscosity to the speed of sound times the scale height h, r_d is the half-mass radius of the disk, and Ω is the angular speed. However, an α-disk prescription assumes the disk is thin relative to its spatial extent, and this assumption is not valid for the disks observed in our simulations. In fact, for the disk observed in simulation 5, $h/r_d \approx 0.1$; far to thick a disk for α-disk accretion rates. As Figure 4.4 shows for an edge-on view of the disk in simulation 5 with the core removed, there remains considerable dense material at high latitudes.

Thin disk accretion severely underestimates the time scale for viscosity driven accretion in these disks. Instead, cooling from conduction and radiation will probably be the dominant evolutionary process over viscous torque for some time. As it cools, conservation of angular momentum will drive it toward becoming a thin disk, shortening the time scale for accretion until viscosity driven accretion becomes the dominant process. However, during cooling, $\approx 0.15\,M_\odot$ of
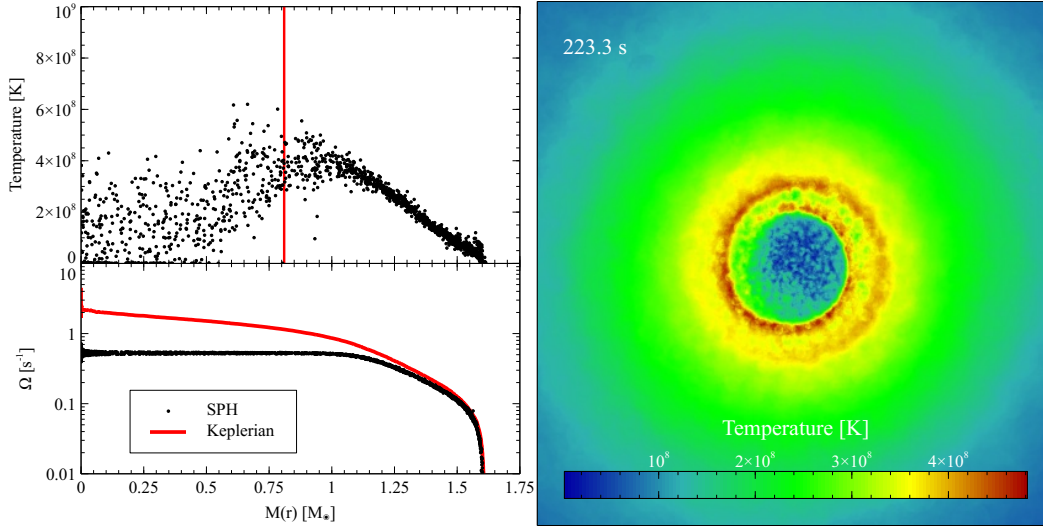
Figure 4.3: Left Panel: Temperature and angular velocity as functions of mass coordinate for the remnant configuration of simulation 4, $0.8\,M_\odot \times 2$ at 223.3s after complete destruction of the secondary. The red vertical line indicates the progenitor mass of the primary star. Right Panel: A slice in the x-y plane of the temperature of the remnant.
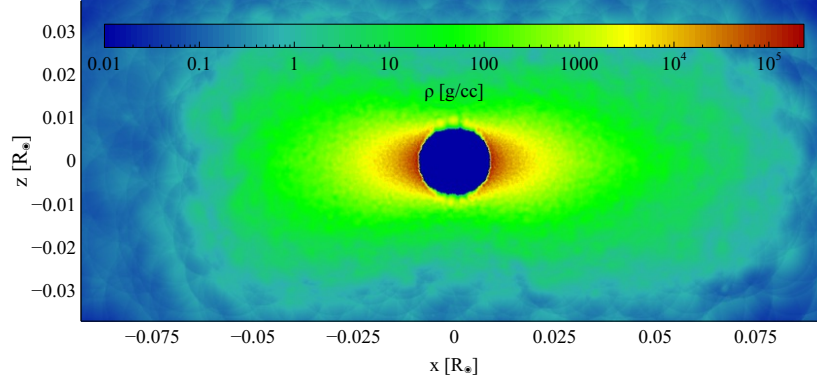
Figure 4.4: An slice through the x-z plane of the disk remnant in simulation 5, $0.81\,M_\odot \times 2$, with the core removed.

gas will have too little angular momentum to remain in orbit, and absent the pressure support from the heated disk, this material will accrete onto the core merely from kinematics, bringing its total mass to $\approx 1.2\,M_\odot$. In the cases where this cooled core mass is super-Chandrasekhar, the final evolution of the core mass no longer depends on disk accretion.

Simulation 8, $0.96\,M_\odot \times 2$, exhibited very much the same behavior as simulation 5, with $0.81\,M_\odot \times 2$. Here, the increased densities of the constituent stars and faster orbital velocity resulted in a much stronger shock, as shown in Figure 4.5. This stronger shock heats some of the material to $\approx 2 \times 10^9$ K in a very similar fashion to the simulation studied in Pakmor

et al. (2010). However, as evidenced by subsequent snapshots, this shock-heated gas simply expands and cools, joining the flow of material into the disk before setting off a self-initiated detonation. Since our simulations cannot resolve the relevant length-scales at which a detonation might be sustained under these conditions, it remains an open question as to whether a prompt detonation is a natural outcome here.
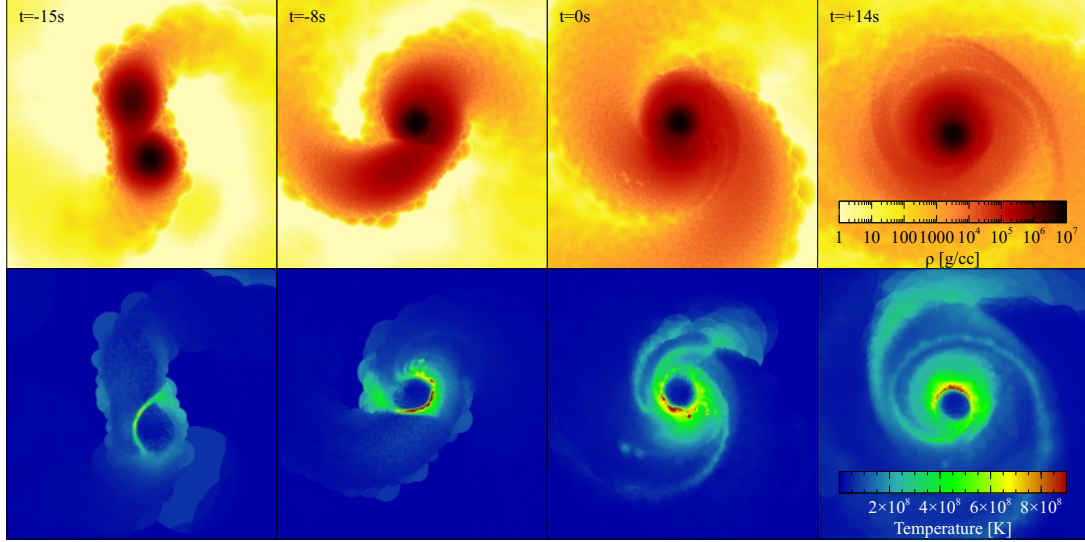
Figure 4.5: Same as figure 4.2, but for simulation 8, $0.96\,M_\odot \times 2$.

As Figure 4.6 demonstrates, the remnant core is slightly colder and the core-disk interface is slightly hotter than the remnant in simulation 5. This implies that while the shock heating of the disk and interface was stronger, the shock was less able to penetrate through the primary star. In fact, the core of the primary remains essentially unchanged from its original state.

More importantly, the fraction of the disk that would rapidly accrete onto the core during cooling and before viscous torque becomes important is sufficient to bring the core mass to $\approx 1.44\,M_\odot$ which is above the Chandrasekhar limit. It is an open question as to whether a white dwarf pushed to the Chandrasekhar limit through this type of accretion will result in a SNIa or in accretion induced collapse to a neutron star. Whichever path this core mass takes, it will do so independently of the disk evolution.

For simulation 1, $0.64\,M_\odot \times 2$, the common-envelope phase is foreshortened, and unlike the more massive pairs of equal-mass white dwarfs, the cores of both stars merge at the center of mass, as depicted in Figure 4.7. This is most likely due to the stars being less massive and
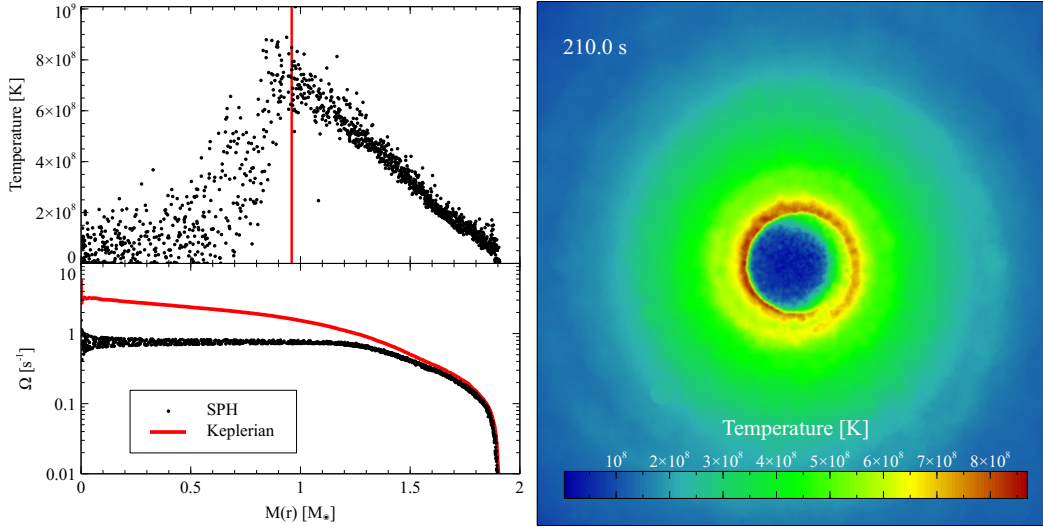
Figure 4.6: Same as figure 4.3, but for simulation 8, $0.96\,M_\odot \times 2$ at 210.0s after the destruction of the secondary.

thus, more susceptible to tidal disruption.
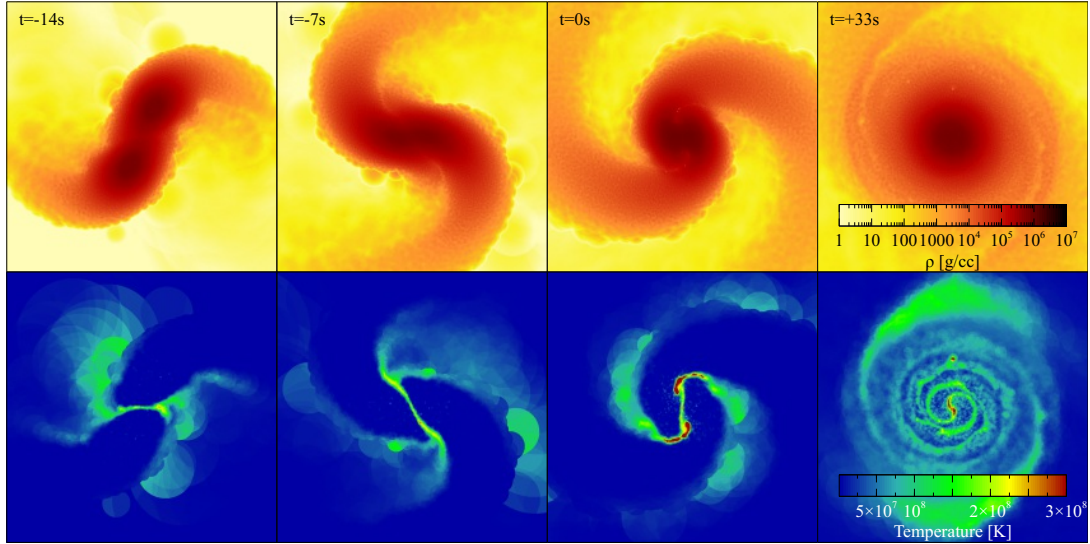
Figure 4.7: Same as figure 4.2, but for simulation 1, $0.64\,M_\odot \times 2$.

The merged core of the remnant in simulation 1 has a temperature of $\sim 2 \times 10^8$ K and exhibits solid-body rotation out to $\approx 0.84\,M_\odot$. After cooling, this core will have a mass of $\approx 0.99\,M_\odot$. Roughly 80% of the initial helium is burned to carbon and oxygen in this simulation, and with $0.03\,M_\odot$ of helium remaining in the disk, sub-Chandrasekhar detonation mechanisms that require helium atmospheres may still be viable for this system, but this scenario seems unlikely.

For unequal mass simulations, the least massive star is always disrupted entirely, forming an accretion disk around the primary. This is not unlike the equal mass simulations with the more massive constituent stars. However, for mass pairs that involved a $1.06\,M_\odot$ primary, the accretion stream shock on the surface of the primary was sufficiently strong to sustain a helium detonation. This is most clearly evident in simulation 9, $0.96\,M_\odot + 1.06\,M_\odot$, depicted in Figure 4.8. This detonation propagates a shock through the $1.06\,M_\odot$ primary, raising its core temperature slightly and expanding its outer layers on the opposite side of the accretion shock. The detonation shock joins the accretion shock in the accretion stream and stalls as the material there is moving at near the sound speed onto the primary. The energy released from this detonation is $\sim 10^{49}$ erg, however, the detonation was not sufficiently energetic to burn carbon in considerable quantities, or to unbind the primary star.

Figure 4.8: Same format as Figure 4.2, but for simulation 9, $0.96\,M_\odot + 1.06\,M_\odot$, with the time coordinate centered on the moment of the helium detonation. The white arrow in the left-most, lower panel indicates the location of the detonation nucleus. A detonation shock can be seen propagating to the right of this location, through the $1.06\,M_\odot$ primary, expanding its outer layers.

Except for the helium detonation, simulation 9 proceeds in a very similar fashion to the equal mass simulations already discussed. While the $0.96\,M_\odot$ secondary is entirely disrupted into an accretion disk, the core of the $1.06\,M_\odot$ primary is largely unchanged, though slightly heated by the detonation shock. As shown in Figure 4.9, the core-disk interface is much hotter than previous simulations, reaching a maximum temperature of 1.25×10^9 K. The core exhibits solid-body rotation out to $\approx 1.23\,M_\odot$, and after disk cooling, will mass $1.42\,M_\odot$.
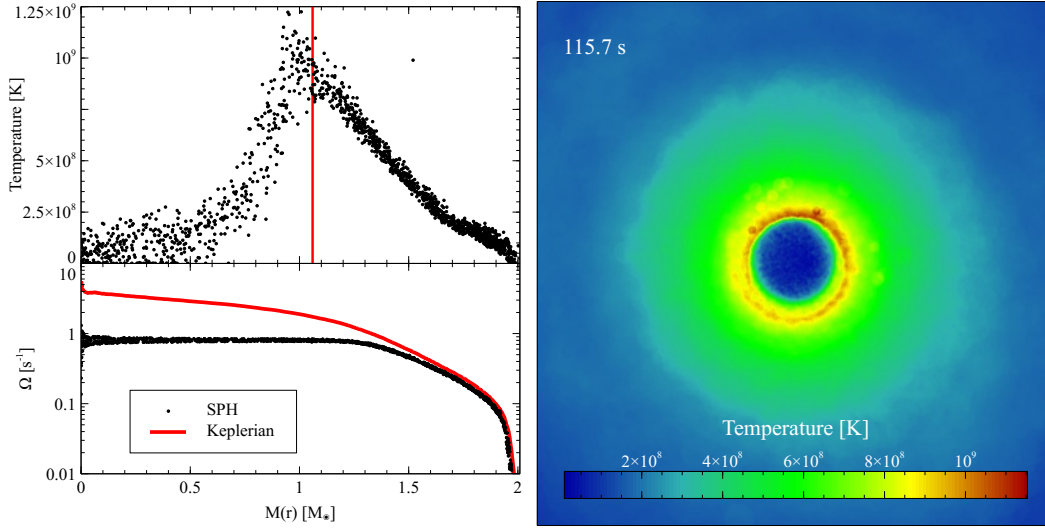
Figure 4.9: Same as figure 4.3, but for simulation 9, $0.96\,M_\odot + 1.06\,M_\odot$, at 115.7s after the destruction of the secondary.

Simulations 4 and 7, $0.64\,M_\odot + 1.06\,M_\odot$ and $0.81\,M_\odot + 1.06\,M_\odot$, both featured these helium detonations as well. The detonation for simulation 4 is illustrated in Figure 4.10. As in simulation 9, $0.96\,M_\odot + 1.06\,M_\odot$, the detonation propagated a shock through the primary, expanding its outer layers, but it did not significantly affect the remnant properties or the formation of a disk. The properties of the disk in this simulation and of the disks in each of our simulations are given in Table 4.2.
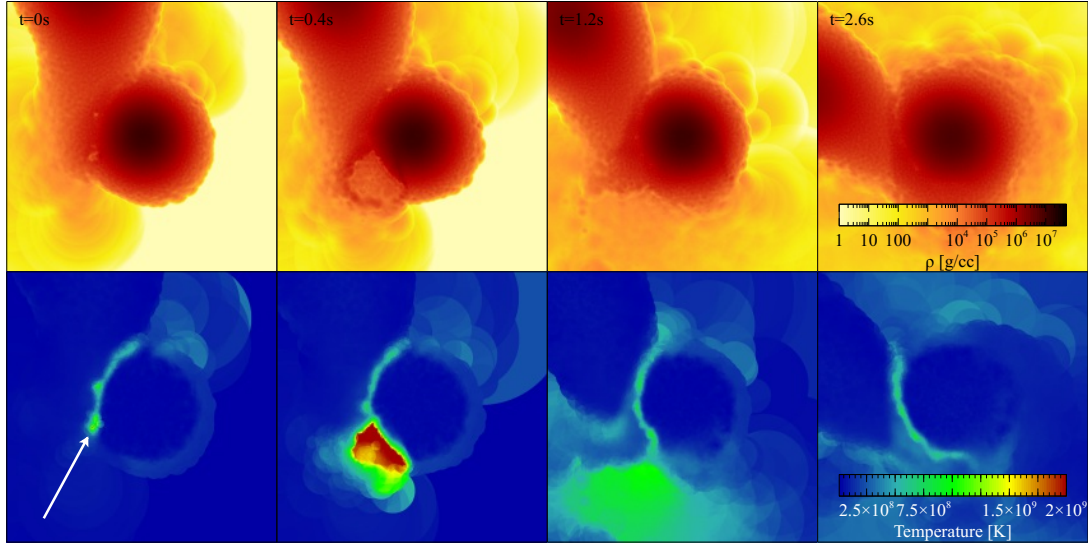

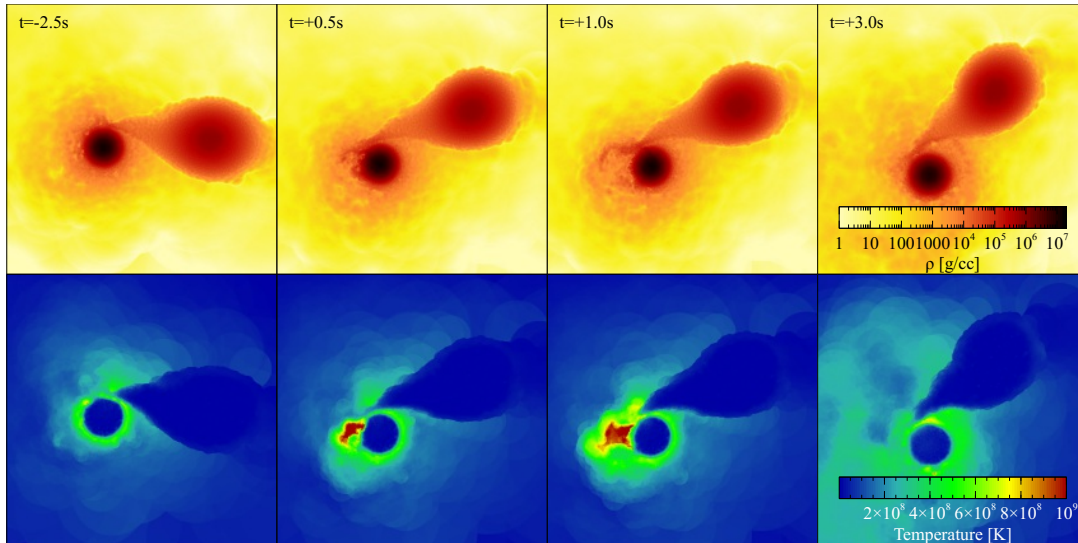
Figure 4.10: Same format as Figure 4.2, but for simulation 4, $0.64\,M_\odot + 1.06\,M_\odot$, with the time coordinate centered on the moment of the helium detonation. A detonation shock propagates to the right, through the $1.0\,M_\odot$ primary, expanding its outer layers.

Table 4.2: Simulated binary mass pairs and their disk properties. M_* is the final mass of the core after the inner disk cools, but before viscosity driven disk accretion. The half-mass radius of the disk is given as r_d. Ω is the rotational speed of the inner disk. All units are solar unless specified otherwise.

#	m_1	m_2	M_{disk}	M_{core}	M_*	r_d	Ω [s^{-1}]
1	0.64	0.64	0.44	0.84	0.99	0.019	0.36
2	0.64	0.81	0.49	0.96	1.05	0.023	0.38
3	0.64	0.96	0.53	1.07	1.16	0.028	0.45
4	0.64	1.06	0.59	1.11	1.20	0.029	0.46
5	0.81	0.81	0.57	1.05	1.20	0.019	0.47
6	0.81	0.96	0.67	1.10	1.26	0.020	0.57
7	0.81	1.06	0.75	1.12	1.30	0.019	0.69
8	0.96	0.96	0.67	1.25	1.44	0.016	0.67
9	0.96	1.06	0.79	1.23	1.42	0.017	0.78

4.4 Discussion

Double degenerate progenitor scenarios are quickly drawing new interest among the astrophysical community. They have the potential to explain many of the confounding mysteries that remain about SNeIa, and to enhance their usefulness as cosmological probes. Here, we have conducted a large simulation survey of white dwarf binary mergers in order to begin to understand how these systems evolve, and to piece together some of the observational signatures of double degenerate SNeIa.

In each of our simulations, the merger remnant consisted of a cold, degenerate core surrounded by a hot accretion disk. These disks were thick, relative to their half-mass radii ($h/r_d \sim 0.1$), and so α-disk accretion rates are not appropriate for them. Given the structure of the disks we observed, cooling time scales are most likely the dominant evolutionary processes. For many of our simulations, this implies that a Chandrasekhar mass object will form at the center of mass before viscous accretion of the disk becomes important.

The only exception to this remnant configuration was the simulation of two $0.64\,M_\odot$ white dwarfs, where the cores of both stars merged at the center of mass, heating the remnant core considerably and lifting most of its degeneracy. Since it is unlikely that two identical mass white dwarfs would form in a binary in nature, this scenario might seem of trivial importance, but the merging of the cores was less the result of their masses being identical than it was of the stars being highly susceptible to tidal disruption. Our other equal mass simulations with more massive constituent stars featured merger scenarios wherein one of the stars was completely disrupted into an accretion disk around the core of the other. Therefore, it is likely that merger

scenarios involving slightly unequal but low-mass white dwarfs might also exhibit core merging.

While none of our simulations exhibited prompt carbon detonations, all of the simulations that included a $1.06\,M_\odot$ primary did exhibit prompt helium detonations on the surface of the primary. These helium detonations were not sufficiently energetic to significantly burn much of the carbon or to unbind either of the constituent stars, but the detonation shocks they produced did alter the structure of the primary before complete merger. Moreover, at $\sim 10^{49}$ ergs, the energy these detonations released is likely sufficient to be observable by many of the upcoming transient surveys, such as LSST.

Whether white dwarf mergers produce SNeIa is still an open question. Our simulations and others' represent only the beginnings of our exploration of this progenitor mechanism. Preliminary results look very promising, and it is doubtless that the viability of mergers as SNeIa progenitors will be established in the near term. Meanwhile, it remains an exciting time to be exploring these dynamical scenarios that continue to surprise us.

Chapter 5

THE FUTURE

In the previous chapter, we explored simulations of white dwarf mergers and examined their remnant configurations. With one notable exception, all of these simulation remnants featured a cold, degenerate core surrounding by a hot accretion disk. We discussed attempts made by other groups to estimate the evolution of these disks using α-disk viscosity. Since the disks we observed were much too thick for thin disk approximations to be valid, we concluded that these were not in fact α-disks, and that the cooling processes are the dominant evolutionary processes for these disks.

This conclusion naturally leads to the question of how then these disks will actually evolve, since viscosity of some unknown quantity must still play a role as the disk cools. Moreover, while we concluded in the previous chapter that some of the remnant cores will grow to Chandrasekhar masses during the cooling phase, we could not say whether this would lead to SNeIa or to accretion induced collapse to a neutron star. Nor could we make many conclusions about the observable signatures of the helium detonations we observed in some of the mergers. In this chapter, we lay out the future avenues and research programs that will attempt to answer some of these remaining questions about white dwarf mergers.

5.1 Implicit-Explicit Evolution in SNSPH

As discussed and demonstrated in previous chapters, SNSPH is an exquisite tool for modeling dynamical progenitor scenarios. Its natural ability to conserve angular momentum makes it the ideal tool for modeling mergers and accretion disks. However, a weakness that it shares with all explicit hydrodynamical codes is its inability to operate on time scales longer than the CFL condition ($t_{CFL} \approx \Delta x/c_s$). This is perfectly valid for simulations where the dynamical time scales are of the same order as the hydrodynamical time scales, but as was observed in our merger simulations in the previous chapter, the system settled into a nearly stable state where dynamical changes were bound to operate on much longer time scales than the hydrodynamics or the CFL condition would dictate. In that scenario, the relevant time scale is the Kelvin-Helmholtz or cooling time scale, t_{KH}. This is typically on the order of 10^{10} dynamical times and is far too large to simulate with an purely explicit code.

The alternative that is often used under these conditions is an implicit hydrostatic solver

that assumes hydrostatic equilibrium at all times throughout the simulation and only evolves the relevant thermodynamics. In this scenario, such a simulation would operate on Kelvin-Helmholtz time scales, solving for hydrostatic equilibrium at each time step, and eliminating kinematics from the simulation entirely. Without kinematics, such a simulation would require a prescribed viscosity of some sort that is typically approximated via a tunable accretion rate. It is also typical for these simulations to operate in one or two dimensions, since absent any dynamics, a hydrostatic calculation does not gain any precision by operating in full 3D.

A implicit hydrostatic code would seem like a natural avenue for iterating our merger remnants forward. However, there are a number of drawbacks to taking this approach. First, since remnants are the result of an explicit particle code, and since nearly all implicit codes use a grid-based resolution method, the remnant configurations would need to be adapted to the new code's preferred resolution framework. Moving from particles to grid cells necessarily involves interpolation, and thus, a loss of resolution. Second, since most implicit codes operate in fewer than three dimensions, the full geometry of the accretion disk would be sacrificed. And third, without kinematics, the viscous torque leading to angular momentum loss would be purely prescriptive rather than an emergent property of the physics of the disk. If the angular momentum loss is purely by prescription, the observed accretion rate becomes a tunable knob that can be set for a desired outcome.

Instead, we plan to integrate some of the implicit physics that operates on very long time scales into SNSPH in order to preserve geometric and dynamical parity with the results of the hydrodynamic calculations. To accomplish this, we have built into SNSPH a bookkeeper module that tracks two time scales simultaneously, Δt_{dyn} and Δt_{long}. This bookkeeper takes account of the contributions to the time derivative of internal energy (u) from long time scale processes like conduction and radiation and adjusts Δt_{long} to optimize the evolution of the most rapid physical process. The unitless quantity $\xi = \Delta t_{long}/\Delta t_{dyn}$ is then used to scale any of the other relevant, non-dynamical processes to maintain parity.

For instance, to account for energy exchange in the disk via conduction, we have implemented an energy diffusion term of the form

$$\Delta u_i = \xi \Delta t_{dyn} \sum_j \frac{m_j}{\rho_i \rho_j} \frac{(\kappa_j + \kappa_i)(T_j - T_i)}{|\mathbf{r}_{ij}|^2} \mathbf{r}_{ij} \nabla_i W_{ij}, \tag{5.1}$$

where i and j are particle indices, m is mass, ρ is density, κ is conductive opacity, T is temper-

ature, and $\nabla_i W_{ij}$ is the gradient of the smoothing kernel of particles i and j at a distance of $\mathbf{r}_{ij}$. The scaling quantity, ξ, is determined by an optimization in the change in energy such as $\Delta u_{cond}/u < 0.1$. If the radiation time scale is longer than the conduction time scale, the change in energy from radiation which takes the form

$$\Delta u_i = \xi \Delta t_{dyn} \sigma T_i^4 A, \tag{5.2}$$

where σ is the Stephan-Boltzmann constant and A is the exposed surface area of a radiating particle, will scale to the diffusion time scale, and vice versa. The bookkeeper module ensures that none of the long time scale physical processes overtake one another while also allowing those processes to run at significantly accelerated rates over the dynamical time scales that govern the kinematics of the simulation.

A necessary pre-condition for this method to remain viable is the complete absence of any sound waves in the system. Since sound waves will evolve on dynamical time scales, this method will drastically overestimate the effect of the long time scale physics on the sound wave's evolution, potentially dissipating their energy in an unreasonable fashion. In modeling accretion disks, however, we do not expect to encounter any sound waves.

Conduction and heat diffusion are already implemented and working in our modified version of SNSPH. Figure 5.1 demonstrates the result of a proof-of-concept test wherein a nearly infinite rod is given a constant temperature at one end and the heat energy diffuses along the length of the rod on long time scales. In this case, the rod had a cross-sectional radius of $0.01 R_\odot$, the approximate radius of a white dwarf star, and densities commensurate with what is found in the cores of white dwarfs.

As is evident from Figure 5.1, our bookkeeper module is able to run a simulation out to $\sim 10^{12}$ dynamical times, and our conduction/diffusion routine matches analytical models quite well. What remains is an implementation of a viscosity that strikes the right balance between prescription and emergent physics, and to scale that viscosity, whichever form it may take, with the bookkeeper scaling quantity ξ. Once the implementation of viscosity is complete, we will have all the relevant physical processes we need to advance our merger remnants forward in time and observe their final outcomes. Whether merger remnants result in SNeIa or in neutron stars, a simulation study of this kind will be the first to attempt to answer this question with explicit rigor.
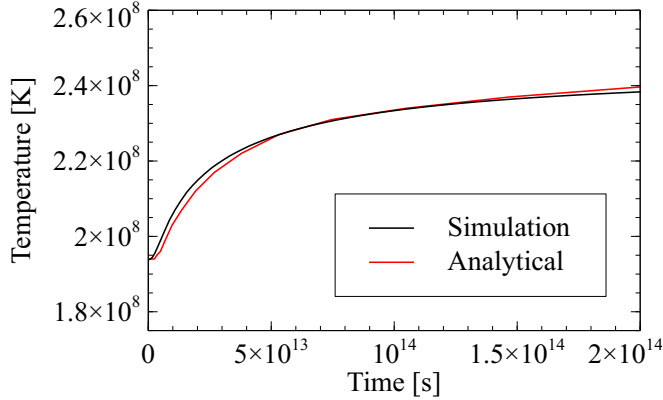
Figure 5.1: Comparisons between our simulation and the analytical prediction of the temperature evolution of a single location on an nearly infinite rod with a constant temperature at one end.

5.2   Radiative Transfer

In the previous chapter, we observed that each of the unequal mass merger simulations that featured a $1.06\,M_\odot$ primary exhibited a helium detonation on the surface of the primary. These detonations released $\sim 10^{49}$ ergs in ≈ 0.5 s, and were sufficiently energetic to alter the structure of the primary. Such an explosion would almost certainly be visible to ground telescopes and transient sky surveys, and it bears all the hallmarks of a helium nova, such as V445 Puppis (Kato & Hachisu 2003). The current understanding of helium novae employs compact white dwarfs accreting helium from evolved, non-degenerate companions. If, indeed, we have discovered a new mechanism for producing helium novae, we would like to make predictions of their particular spectra and light-curves so as to distinguish observed helium novae as stemming from the traditional picture or from our new model.

In order to do this, we will employ a radiative transfer code called PHOENIX (Baron et al. 2009). This atmosphere code is fully relativistic and generalizable to three dimensions. With this code, we will be able to construct detailed spectra of these explosions and compare them to helium novae observations. We will also be able to construct light-curves which are often the only available observations of transients. These light-curves will tell us how bright the explosions appear and how long they last. Armed with this information, we should be able to make testable predictions of how often these events should be observed by various transient searches.

70

5.3   Other Progenitor Mechanisms

The well of information about SNeIa progenitors has not yet been tapped. Here, we have explored mostly double degenerate mechanisms, but there are a number of outstanding questions that remain, even in the more ordinary case of a single white dwarf in a binary with a non-degenerate companion. For instance, it is still not clear how accretion produces a supernova, since a white dwarf reaching the Chandrasekhar limit does not imply a catastrophic, thermonuclear detonation must necessarily result. It is also unclear how all of the hydrogen that typically persists in evolved companions nevertheless does not appear in SNeIa spectra.

The search for robust progenitor mechanisms will go on, and undoubtedly, the astrophysical community will uncover peculiar, previously unthought of mechanisms. Already, considerable effort is being expended exploring sub-Chandrasekhar detonation models. This and other mechanisms will likely occupy astrophysicists for some time, and we may never arrive at a satisfactory explanation of every peculiar feature of SNeIa. The Universe appears not to be very picky about how it accomplishes things, like blowing up white dwarfs, since SNeIa are quite common. The Universe simply does what it does, and we in the scientific community will likely always have plenty of work to do, explaining what we think is happening, and hoping, perhaps, that we might be right - some of the time.

REFERENCES

Anderson, J. P., James, P. A., Salaris, M., & Percival, S. M. in Supernovae 1987A: 20 Years After – Supernovae and Gamma-Ray Bursters (eds Immler, S. & Weiler, K.) 220-224 (AIP, 2007).

Anderson, J. P. & James, P. A. 2008, MNRAS, 390 1527

Arnett, D. 1994, AAS, 184, 5003

Aubourg, É et al. 2008, A&A, 492, 631

Barbon et al. 1999, A&AS, 139, 531

Baron, E., Chen, B., & Hauschildt, P. 2009, preprint at (http://arXiv.org/abs/0908.4273)

Benz, W., Cameron, A. G. W., & Bowers, R. L. 1989a, LNP, 328, 511

Benz, W., Thielemann, F.K., & Hills, J.G., 1989b, ApJ, 342, 986

Binney, J. & Tremaine, S. 1987, Galactic Dynamics, Princeton University Press

Branch, D. & Tammann, G. A. 1992, ARA&A, 30, 359

Brodie, J., Strader, J. 2006, ARA&A, 44, 193

Bruzual, G. & Charlot, S. 2003, MNRAS, 344, 1000

Chabrier, G. 2003, PASP, 115, 763

Chandrasekhar, S. 1931, ApJ, 74, 81

Chomiuk, L., Strader, J., & Brodie, J. P. 2008, AJ, 136, 234

Colgate, S. A. 1979, ApJ, 232, 404

Cooper, M., Newman, J. & Yan, R. 2009, preprint at (http://arXiv.org/abs/0901.4338)

Conley, A. et al. 2008, ApJ, 681, 482

Dahlén, T. et al. 2004, ApJ, 613, 189

Dan, M., Rosswog, S., Guillochon, J., & Ramirez-Ruiz, E. 2011, arXiv, 1101.5132

Diehl, S. & Statler, T. S. 2006, MNRAS, 368, 497

Dilday, B. et al. 2008, ApJ, 682, 262

Dursi, L. J. & Timmes, F. X. 2006, ApJ, 641, 1071

Eggleton, P.P., 1971, MNRAS, 151, 351

Feltzing, S., Holmberg, J., & Hurley, J. R. 2001, A&A, 377, 911

Fickett, W. & Davis, W. C. 1979, Detonation (Berkeley: University of California Press)

Fruchter, A.S., et al. 2006, Nature, 441, 463

Fryer, C. L., Rockefeller, G., & Warren, M. S. 2006, ApJ, 643, 292

Fryxell, B. et al. 2000, ApJS, 131, 273

Gallagher, J. S. et al. 2008, ApJ, 685, L752

Gal-Yam, A. & Maoz, D. 2004, MNRAS, 347, 942

Gasques, L.R. et al. 2007, Phys. Rev. C. 76, 035802

Goldreich, P. & Tremaine, S. 1981, ApJ, 243, 1062

Greggio, L. & Renzini, A. 1983, A&A, 118, 217

Greggio, L. 2005, A&A, 441, 1055

Hamuy, M. et al. 1996, AJ, 112, 2391

Herwig, F., 2004, ApJ, 605, 425

Hicken, M., Garnavich, P. M., Prieto, J. L., Blondin, S., DePoy, D. L., Kirshner, R. P., &
    Parrent, J. 2007, ApJ, 669, L17

Hillebrandt, W., & Niemeyer, J. C. 2000, ARA&A, 38, 191

Howell, D. A. et al. 2000, ApJ, 530, 166

Howell, D. A. 2001, ApJ, 554, L193

Howell, D. A. et al. 2006, Nature, 443, 308

Howell, D. A., Sullivan, M., Conley, A., & Carlberg, R. 2007 ApJ, 667L, 37

Hoyle, F. & Fowler, W. A. 1960, ApJ, 132, 565

Iben, Jr., I., & Tutukov, A. V. 1984, ApJS, 54, 335

Jiang, C.L., et al. 2007, Phys. Rev. C 75, 015803

Kato, M. & Hachisu, I. 2003, ApJL, 598, 107

Kelly, P. L., Kirshner, R. P., & Pahre, M. 2008, ApJ, 687, 1201

Khokhlov, A., Müller, E., & Hoeflich, P. 1993, A&A, 270, 223

Kobayashi, C., Tsujimoto, T. & Nomoto, K. 2000, ApJ, 539, 26

Kowalski et al. 2008, ApJ, 686, 749

Krause, O. et al. 2008, Nature, 456, 617

Lorén-Aguilar, P., et al. 2009, A&A, 500, 1193

Lorén-Aguilar, P., Isern, J., & García-Berro, E. 2010, arXiv:1004.4783L

Mannucci, F., et al. 2005, A&A, 433, 807

Mannucci, F., Della Valle, M. & Panagia, N. 2006, MNRAS, 370, 773

Maoz, D. 2008, MNRAS, 384, 267

Marsh, T.R., Nelemans, G., & Steeghs, D. 2004, MNRAS, 350, 113

Mathews, J. 1992, Numerical Methods, 2nd Edition, Prentice-Hall, Inc

McWilliam, A. 1992, ARA&A, 35, 503

Müller, E. 1986, A&A, 162, 103

Nomoto, K. 1982, ApJ, 253, 798

Nomoto, K. & Kondo 1991, ApJL, 367, 19

Nonaka, A. et al. 2010, ApJS, 188, 358

Pakmor, R. et al. 2010, Nature, 463, 61

Perlmutter, S. et al. 1999, ApJ, 517, 565

Peterson, C. & King, J. 1975 AJ, 80, 427

Pfahl, E., Scannapieco, E., & Bildsten, L. 2009, ApJ, 695, L111

Pfannes, J. M. M., Niemeyer, J. C., Schmidt, W., & Klingenberg, C. 2010, A&A, 509, 74

Phillips, M. M. 1993, ApJ, 413, L105

Pritchet, C. J., Howell, D. A. & Sullivan, M. 2008, ApJ, 683, L25

Pskovskii, Iu. P. 1977, Soviet Astron., 21, 675

Raskin, C., Scannapieco, E., Rhoads, J. & Della Valle, M. 2008, ApJ, 689, 358

Raskin, C., Timmes, F.X., Scannapieco, E., Diehl, S., & Fryer, C. 2009, MNRAS, 399, 156

Raskin, C., Scannapieco, E., Rockefeller, G., Fryer, C., Diehl, S., & Timmes, F.X. 2010, ApJ, 724, 111

Riess, A. G. et al. 1998, AJ, 116, 1009

Rosswog, S., Kasen, D., Guillochon, J., & Ramirez-Ruiz, E. 2009 ApJL, 705, 128

Salpeter, E. 1955, ApJ, 121, 161

Scalzo, R. A. et al. 2010, ApJ, 713, 1073

Scannapieco, E. & Bildsten, L. 2005, ApJ, 629, L85

Shakura, N. & Sunyaev, R. 1973, A&A, 24, 337

Starrfield, S., Sparks, W. M., Truran, J. W., & Wiescher, M. C. 2000, ApJS, 127, 485

Strigari, L. E. 2006, New Astronomy Review, 50, 566

Shaw, R.L. 1979, A&A, 76, 188

Sullivan, M. et al. 2006, ApJ, 648, 868

Timmes, F. X., Woosley, S. E., & Weaver, T. A. 1995, ApJS, 98, 617

Timmes, F. X. 1999, ApJs, 124, 241

Timmes, F. X. & Arnett, D. 1999, ApJs, 125, 277

Timmes, F. X. & Swesty, F. D. 2000, ApJs, 126, 501

Timmes, F. X., Hoffman, R. D., & Woosley, S. E. 2000, ApJs, 129, 377

Timmes, F. X., Brown, E. F. & Truran, J. W. 2003, ApJ, 590, L83

Totani, T., Morokuma, T., Oda, T., Doi, M., & Yasuda, N. 2008, PASJ, 60, 1327

van den Bergh, S., Li, W. & Filippenko, A. V. 2005, PASP, 834, 773

Weaver, T.A., Zimmerman, G.B., & Woosley, S.E., 1978, ApJ, 225, 1021

Webbink, R. F. 1984, ApJ, 277, 355

Wheeler, J. C., Sneden, C., & Truran, Jr., J. W. 1989, ARA&A, 27, 279

Whelan, J., & Iben, I. J. 1973, ApJ, 186, 1007

Williams, K., Bolte, M., & Koester, D. 2004, ApJL, 615, 49

Yoon, S.-C. & Langer, N. 2004, A&A, 419, 645

Yoon, S.-C. & Langer, N. 2005, A&A, 435, 967

Yoon, S.-C., Podsiadlowski, P., & Rosswog, S. 2007, MNRAS, 380, 933

Young, P. A., & Arnett, D., 2005, ApJ, 618, 908